Article

https://doi.org/10.1038/s41593-023-01327-2

# Glymphatic influx and clearance are accelerated by neurovascular coupling

Stephanie Holstein-Rønsbo[1,4], Yiming Gan [2,4], Michael J. Giannetto [3], Martin Kaag Rasmussen[1], Björn Sigurdsson [1], Felix Ralf Michael Beinlich [1], Laura Rose[1], Verena Untiet [1], Lauren M. Hablitz [3], Douglas H. Kelley [2] & Maiken Nedergaard [1,3] ✉

Functional hyperemia, also known as neurovascular coupling, is a phenomenon that occurs when neural activity increases local cerebral blood flow. Because all biological activity produces metabolic waste, we here sought to investigate the relationship between functional hyperemia and waste clearance via the glymphatic system. The analysis showed that whisker stimulation increased both glymphatic influx and clearance in the mouse somatosensory cortex with a 1.6-fold increase in periarterial cerebrospinal fluid (CSF) influx velocity in the activated hemisphere. Particle tracking velocimetry revealed a direct coupling between arterial dilation/ constriction and periarterial CSF flow velocity. Optogenetic manipulation of vascular smooth muscle cells enhanced glymphatic influx in the absence of neural activation. We propose that impedance pumping allows arterial pulsatility to drive CSF in the same direction as blood flow, and we present a simulation that supports this idea. Thus, functional hyperemia boosts not only the supply of metabolites but also the removal of metabolic waste.

Neurons have little storage of energy metabolites and are, therefore, dependent upon the tight coupling of neural activity with blood flow. Upon stimulation, the need for energy metabolites heightens and cerebral blood flow increases promptly to supply oxygen and glucose in the process called neurovascular coupling[1]. However, the large increase in cerebral blood flow surpasses the metabolic need for oxygen, leading to the speculation that functional hyperemia may serve additional roles[2]. An elegant neuroimaging study documented that brain-wide functional hyperemia induced by oscillatory increases in neural activity during sleep drives cerebrospinal fluid (CSF) inflow into the fourth ventricle[3]. The authors speculated that the reciprocal interchange of blood and CSF volumes within the rigid cavity of the skull was responsible for initiating the distant movement of CSF.

Here we hypothesize that vasodilation induced by sensory stimulation accelerates CSF flow in addition to increasing local blood flow. We used minimally invasive procedures along with quantitative fluid dynamic approaches to map the effects of functional hyperemia on the glymphatic influx and efflux. Kinetic analysis based on tracking the transport of fluorescent microspheres in the pial perivascular spaces (PVSs) allowed a direct correlation of changes in vascular diameter with CSF flow velocity. Moreover, cell-specific optogenetic stimulation enabled the first test of the importance of neural versus vascular activity. The main conclusion reported here is that dynamic changes in vascular diameter drive perivascular glymphatic CSF inflow and clearance, and that CSF inflow can occur in the absence of neural activation.

## Results

### Whisker stimulation causes functional hyperemia

Whisker stimulation activates barrel cortex neurons along with an increase in local blood flow[4], and the magnitude of functional hyperemia is determined by the stimulation parameters[5,6]. To validate our model and optimize our stimulation protocol, we applied different

[1]Center for Translational Neuromedicine, University of Copenhagen, Copenhagen, Denmark. [2]Department of Mechanical Engineering, University of Rochester Medical Center, Rochester, NY, USA. [3]Center for Translational Neuromedicine, Division of Glial Disease and Therapeutics, University of Rochester Medical Center, Rochester, NY, USA. [4]These authors contributed equally: Stephanie Holstein-Rønsbo, Yiming Gan. ✉e-mail: nedergaard@sund.ku.dk

regimens of unilateral whisker stimulation to GCaMP-reporter mice to identify the area and extent of neuronal activation, as well as hemodynamic changes. Local field potential (LFP) is commonly used to assess neural activity, but the insertion of the LFP electrodes will suppress glymphatic flow by ~70–80%[7]. We, therefore, took advantage of $Ca^{2+}$ imaging in Thy1-GCaMP6S reporter mice, which noninvasively report neural activity[8]. Both $Ca^{2+}$ imaging and intrinsic optical imaging (IOS) demonstrated that cortical activation was restricted to the barrel cortex of the contralateral hemisphere[9,10] (Fig. 1b, Extended Data Fig. 1a–c and Extended Data Fig. 1g–h). During baseline recording without whisker stimulation, only minor hemodynamic changes reflecting spontaneous activity were observed (Extended Data Fig. 1i). In anesthetized (ketamine/xylazine (KX)) Thy1-GCaMP6S reporter mice, a 5 Hz stimulation protocol with 10 ms pulses (190 ms interval) produced the most reliable response (Fig. 1c and Extended Data Fig. 1d–f), in accordance with previous reports[11,12]. The GCaMP fluorescence was not corrected for the time-varying effects of hemoglobin absorption, thus $Ca^{2+}$ signals can be observed below baseline (Fig. 1c)[13]. Laser-Doppler flowmetry confirmed that the stimulation protocol was associated with the largest amplitude elevation of blood flow, thus supporting the notion that functional hyperemia is tightly linked to the intensity of neural activation (Fig. 1c). Based on this analysis, we therefore proceeded with a whisker stimulation protocol of 5 Hz with 10 ms pulses (10 psi) for periods of 30 s intersected by 60 s intervals with no stimulations.

### Functional hyperemia increases the glymphatic influx

To examine the effect of functional hyperemia on the glymphatic influx, we combined repeated whisker stimulations with in vivo imaging through the intact skull of CSF tracer transport (70 kDa dextran) under KX anesthesia (Fig. 1a). Approximately 10 min after intracisternal injection, the tracers appeared at the trunk of the middle cerebral artery (MCA) in both hemispheres, at which point air-puffs were used to stimulate the whiskers. Earlier mice studies have shown that glymphatic tracer inflow typically dominates during the first ~30 min, whereafter the tracer signal starts to decrease reflecting glymphatic efflux[14]. In this influx experiment, the whiskers were unilaterally stimulated for 30 s (5 Hz, 10 ms) every 90 s or over 30 min. CSF tracer signal continuously increased in both hemispheres as the tracer entered the PVS surrounding the MCA and its branches, yet the whisker stimulations consistently triggered a higher net tracer influx compared to the unstimulated hemisphere (Fig. 1d–e and Supplementary Video 1). Thus, sensory stimulation increases glymphatic CSF tracer influx. In a control group, not exposed to whisker stimulation, the tracer signal increased steadily across the imaging period (30 min) with no difference between hemispheres (Extended Data Fig. 2a). Furthermore, the total tracer intensity in the hemispheres of the control group reached the same level of tracer intensity as the unstimulated hemisphere of the experimental group (Fig. 1f).

To detail the effect of whisker stimulation on tracer signal, we averaged across the 20 stimulations per mouse. To account for the changing slope that occurs over time during the influx of the CSF tracer (Fig. 1e), we normalized the tracer signal at stimulation start ($t = 30$ s). Interestingly, the analysis showed that both the stimulation start and cessation had a pronounced effect on the tracer signal. As stimulation starts, the tracer signal transiently decreases (Fig. 1g). As the stimulation ends, the tracer signal increases and continues at a steeper inflow rate than for the unstimulated hemisphere, thus causing a larger inflow of CSF tracer. These changes in tracer signal anticorrelate to increases and decreases of cerebral blood flow (Fig. 1c), consistent with the idea that an inverse relationship between CSF and cerebral blood volume exists[3]. In the control group, there was no change in the tracer signal across the 90 s periods (Extended Data Fig. 2b). When tracking the front of the CSF tracer, we similarly found that the velocity is higher in the stimulated hemisphere (Extended Data Fig. 2c). Of note, front tracking includes tracer movement in both PVSs and parenchyma[15].

### Increased CSF tracer in the neuropil

The glymphatic model includes CSF–interstitial fluid (ISF) exchange between the PVSs and the neuropil[16]. To assess whether the CSF tracer accumulated in the parenchyma of the stimulated hemisphere compared to the unstimulated hemisphere, we analyzed tracer intensity around the MCA at 15 min and 30 min in both hemispheres. The parenchymal influx was assessed by using in vivo macroscopic imaging and placing linear regions of interest (ROIs) around the PVSs of the MCA (Fig. 1h). The analysis showed that after 30 min, substantially more tracer had entered the parenchyma of the stimulated hemisphere (Fig. 1i). Thus, whisker stimulations can increase the CSF–ISF exchange in accordance with the glymphatic model of brain fluid transport.

In a new cohort, we collected brains immediately after 30 min of whisker stimulation and imaged tracer distribution in vibratome slices spanning the barrel field cortex (Fig. 1j). We quantified the CSF tracer signal (mean pixel intensity (MPI)) in each hemisphere. The total tracer signal in each brain was set to 100%, and the distribution between hemispheres was calculated. The analysis showed that more tracer had entered the stimulated hemisphere compared to the unstimulated (Fig. 1k), supporting the notion that functional hyperemia enhances the movement of tracer from the PVS into the parenchyma, as has recently been suggested in computational models of the glymphatic system[17]. In mice not exposed to unilateral whisker stimulation, tracer distribution between hemispheres did not differ (Extended Data Fig. 2d).

### Arterial dilation transiently decreases CSF velocity

To obtain quantitative kinetic data with the high temporal resolution, we next injected fluorescently tagged microspheres (1 μm) into cisterna magna and imaged their transport along the MCA using two-photon high-speed imaging followed by custom-built automated particle tracking analysis (Fig. 2a,b and Supplementary Video 2; previously

---

**Fig. 1 | Functional hyperemia increases periarterial CSF influx. a**, Adult wild-type mice were exposed to unilateral whisker stimulation (30 s each), and macroscopic imaging through an intact skull was used to map neuronal activation ($Ca^{2+}$), hemodynamic signals (IOS) or CSF tracer transport under KX anesthesia. **b,** Whisker stimulation (5 Hz, 10 ms) increased neuronal activity (top) and cerebral blood flow (bottom) only in the contralateral hemisphere. **c**, Left–$Ca^{2+}$ traces from barrel field cortex in response to different whisker stimulation protocols ($n = 7$, five stimulations/mouse). Right–relative changes in cerebral blood flow (CBF) in the MCA area ($n = 7$, five stimulations/mouse). **d**, Representative image of tracer influx around the MCA. Dotted circles, ROIs. **e**, Fluorescence signal (MPI) of the tracer influx (70 kDa dextran; $n = 10$ mice). Gray bars show 30 s whisker stimulation. **f**, Area under the curve (AUC) across 30 min tracer influx for the stimulated (stim and unstim hemisphere, $n = 10$ mice; Fig. 1e) and control group (left and right hemisphere, $n = 7$ mice; Extended Data Fig. 2A). Two-way ANOVA w Tukey's correction, $P = 0.0705$, stim vs. unstim;

$P = 0.0022$, stim vs. left; $P = 0.0006$, stim vs. right. **g**, Change in tracer signal across all 20 stimulations per mouse. Normalized according to tracer intensity at stimulation start ($t = 30$ s). **H**, Analysis of tracer efflux from MCA branches into surrounding tissue at 15 and 30 min after whisker stimulation start. Linear ROIs are located outside the perivascular space. **i**, The intensity profiles of CSF tracer in the tissue surrounding the MCA. Right, AUC of the intensity profiles ($n = 10$). Two-way ANOVA w Sidak correction, $P = 0.0133$, $t = 15$; $P < 0.0001$, $t = 30$. **j**, Parenchymal CSF tracer distribution was analyzed in vibratome sections containing somatosensory cortex. **k**, Left–group overlay of the parenchymal influx of CSF tracer ex vivo. Dashed lines, analyzed regions. Right–percentage distribution of tracer (MPI; 3 kDa dextran) in each hemisphere ($52.8 \pm 1.1\%$ vs. $47.2 \pm 1.1\%$; $n = 7$ mice, eight brain sections/mouse). Two-tailed paired $t$-test, $P = 0.049$. **l**, Linear fit to the first 20 min inflow from Fig. 1e, where tracer influx dominates relative to clearance. Data are represented as mean ± s.e.m. *$P < 0.05$, **$P < 0.01$ and ****$P < 0.0001$. See also Extended Data Figs. 1 and 2 and Supplementary Video 1.

described in ref. 18). The analysis showed that the average perivascular CSF flow velocities before and after whisker stimulation are comparable (17.1 ± 3.5 μm s⁻¹; mean ± s.e.m.; Fig. 2c). These values compare well to previously reported values using a similar methodology (17 ± 2 μm s⁻¹ and 18.7 ± 1.3 μm s⁻¹ (refs. 18,19)). In our observations and in the cited literature, the net CSF flow direction was uniform and always in the same direction as the blood flow.

Whisker stimulation led to an increase in the MCA diameter of 3.3 ± 0.7 μm (resting diameter: 58 ± 3.5 μm, corresponding to 5.7 ± 1% dilation; Fig. 2e–g and Extended Data Fig. 3a). The artery wall of the

MCA moves most rapidly during the dilatory phase, and we found the peak velocity to be 1.1 ± 0.2 μm s⁻¹ (Fig. 2f). During arterial dilation, the downstream velocity of the microspheres transiently decreases (from 17.1 ± 3.5 μm s⁻¹ to 8.8 ± 3.2 μm s⁻¹, or a decrease of 48.5%; Fig. 2h–j and Extended Data Fig. 3b), indicating that perivascular CSF inflow along the MCA is transiently impaired as whisker stimulation expands the arterial diameter. Forward flow is rapidly continued as the dilation of the vessel wall ceases. The change in downstream velocity peaks at 4.4 ± 1.2 s after the start of stimulation (Fig. 2j), shortly after the velocity peak of the vessel wall (2.3 ± 0.2 s after the start of stimulation;
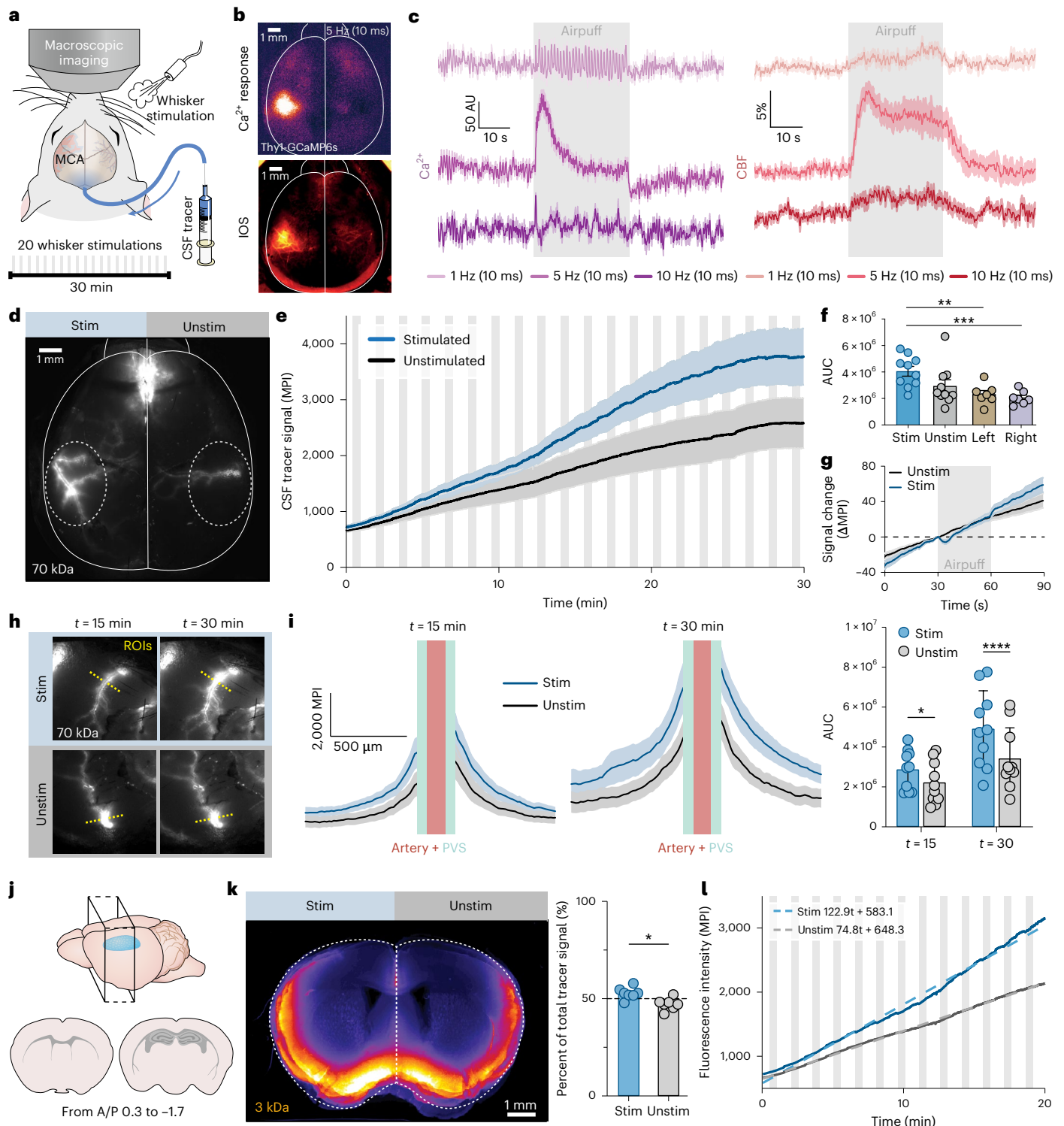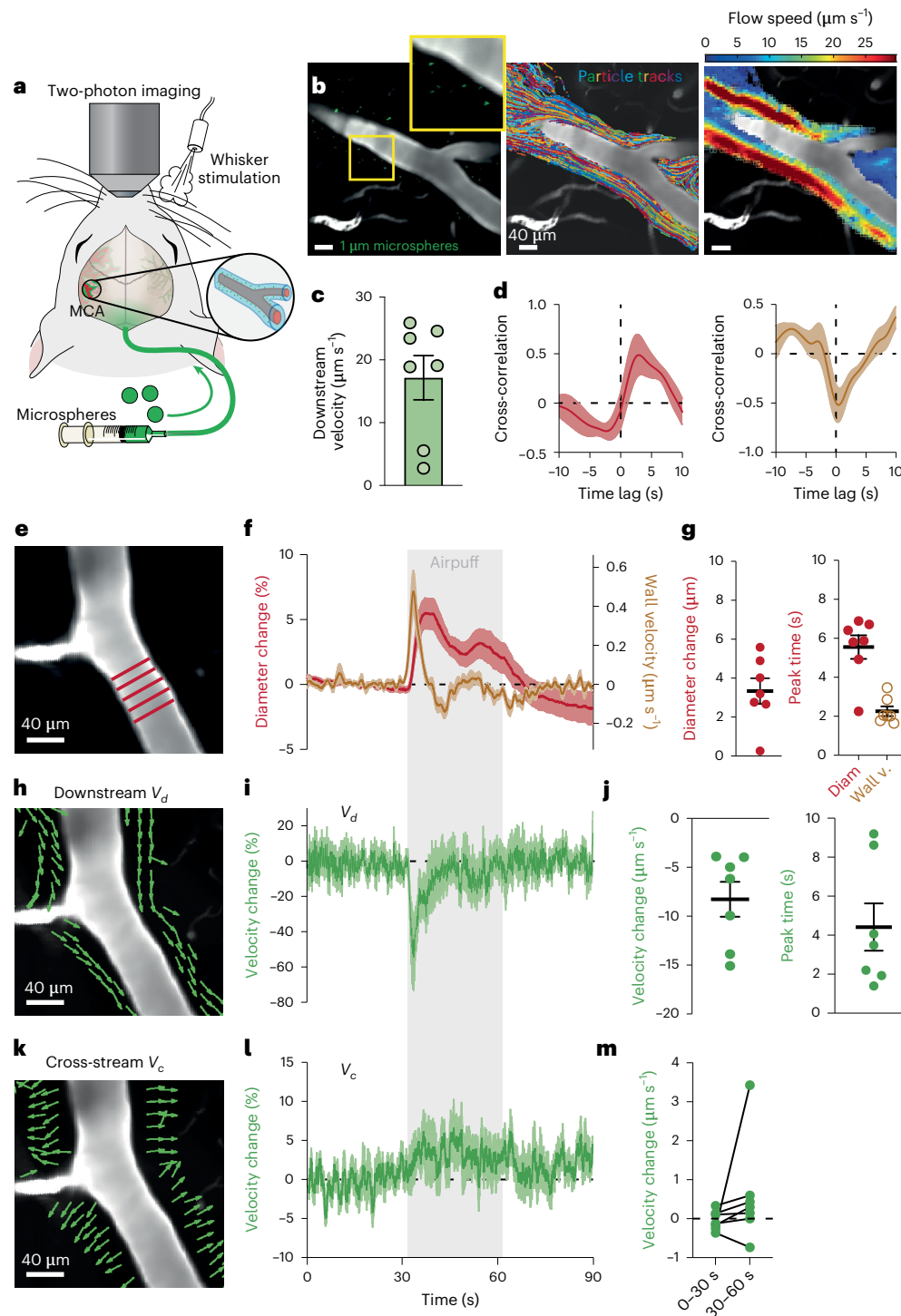
**Fig. 2 | Perivascular CSF flow kinetics is closely controlled by arterial diameter. a**, Adult wild-type mice were head-plated, and a cranial window was inserted above the MCA under KX anesthesia. Microspheres (1 μm) were injected into the cisterna magna before exposure to unilateral whisker stimulation. Two-photon imaging was used to map CSF flow velocity in the perivascular space of the MCA. **b**, The path of fluorescent microspheres in the perivascular space (top left) was tracked (top right) and used to calculate the mean flow speed (bottom). The superimposed trajectories of the tracked microspheres outline the perivascular space. **c**, Average downstream CSF flow velocity in the period before whisker stimulation (n = 7 mice). **d**, Cross-correlation of the downstream CSF flow velocity and artery diameter (left). Cross-correlation of the downstream CSF flow velocity and vessel wall velocity (right) demonstrating little phase difference. **e**, Artery diameter changes were measured and averaged across five linear ROIs spanning the artery lumen. The artery boundaries were automatically registered based on fluorescence intensity. **f**, Percentage artery diameter change (red) and vessel wall velocity (brown) during functional hyperemia (n = 7). **g**, Left—maximum arterial diameter change from baseline. Right—time from stimulation start to peak diameter change (Diam) and peak change in wall velocity (Wall v.; n = 7 mice). **h**, The time-averaged velocity direction field (green arrows) shows net transport in the downstream direction. **i**, Percentage change of downstream velocity ($V_d$) during functional hyperemia (n = 7). **J**, Left—maximum downstream velocity change from baseline. Right—time from stimulation start to peak velocity (n = 7 mice). **k**, The time-averaged velocity direction field (green arrows) shows the net transport in the cross-stream direction. **l**, Percentage change of cross-stream velocity ($V_c$) during functional hyperemia (n = 7). **m**, Average cross-stream velocity during baseline (t = 0–30 s) and stimulation period (t = 30–60 s). Two-tailed paired t-test, P = 0.26. (n = 7 mice). Data are represented as mean ± s.e.m. See also Extended Data Fig. 3 and Supplementary Video 2.
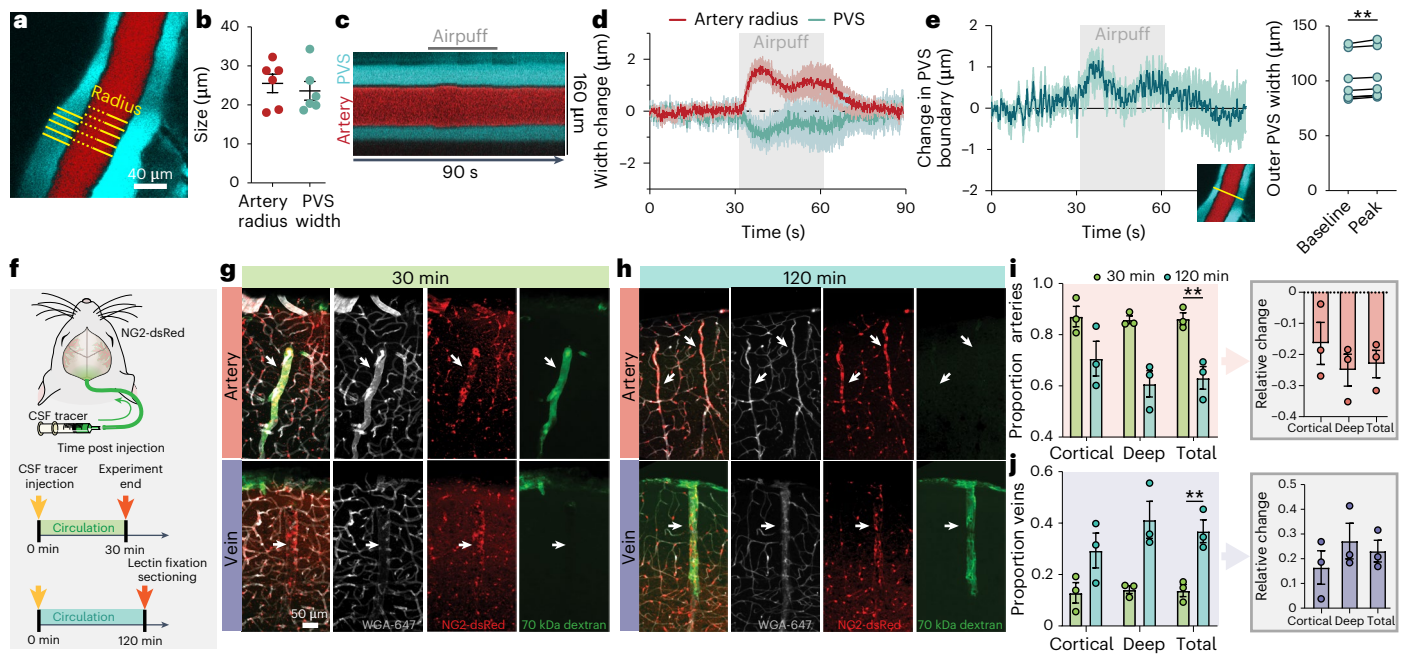
**Fig. 3 | Perivascular spaces—transfer of CSF tracers and dynamic changes.**
**a**, Adult wild-type mice were head-plated, and a cranial window was inserted above the middle cerebral artery under KX anesthesia. CSF tracer (3 kDa dextran) was injected into the cisterna magna before exposure to unilateral whisker stimulation. Two-photon imaging was used to map width changes of artery and perivascular space. The width changes were averaged across five linear ROIs. **b**, Artery radius and PVS width during baseline ($n = 6$ mice). **c,** Kymograph of artery and perivascular space during a 90 s protocol with 30 s stimulation. **d**, Change of arterial radius and perivascular space width during functional hyperemia ($n = 6$). **e**, Movement of the outer perivascular space wall. Right—baseline width and first peak ($n = 7$). Two-tailed paired $t$-test, $P = 0.0015$. **f**, Adult NG2-dsRed mice were intracisternally injected under KX anesthesia. At 30 min or 120 min after injection

start, mice were intracardially perfused with lectin (WGA-647) followed by fixation with 4% PFA. **g**, Cortical CSF tracer distribution at 30 min. Tracer is present along arteries (top, arrow) and absent from veins (bottom, arrow). **h**, Cortical CSF tracer distribution at 120 min. Tracer is less often present along arteries (top, arrow) and more often along veins (bottom, arrow) than at 30 min. **i**, Left—proportion of arteries with CSF tracer at 30 min (green) and 120 min (blue). Right—relative change in total number of arteries labeled with CSF tracer at 120 min compared to 30 min. **j**, Left—proportion of veins with CSF tracer at 30 min (green) and 120 min (blue). Right—relative change in number of veins with CSF tracer at 120 min compared to 30 min. For **i** and **j**, 30 min: $n = 3$ mice, 349 arteries, 52 veins; 120 min: $n = 3$ mice, 384 arteries, 241 veins. Two-tailed paired $t$-test, $P = 0.0099$. Data are represented as mean ± s.e.m. **$P < 0.01$. See also Extended Data Fig. 4.

Fig. 2g), supporting the idea that flow is driven by wall motion[18] (Fig. 2d). In parallel, as the downstream velocity decreases, the cross-stream velocity increases because microspheres move in the direction of the arterial wall motion (Fig. 2k–m and Extended Data Fig. 3c). Overall, this demonstrates that dynamic fluctuations of the arterial diameter are mirrored by changes in the velocity of perivascular CSF inflow. The pressure exerted by arterial dilation appears to transiently reduce the forward movement of the microspheres while driving an increase in cross-stream velocity.

Of note, we observed that damage to the meningeal membranes substantially alters CSF flow—accidental punctures of the membrane surrounding the pial PVS increased the speed of the CSF flow by more than threefold (Extended Data Fig. 3d). To avoid injury to the brain parenchyma, our study was, therefore, based on cisterna magna injection for both tracer and microspheres.

**Artery dilation decreases PVS width**
We speculated the CSF flow velocity changes were brought about by changes in the PVS volume induced by arterial dilation. Through cranial windows, we obtained high-resolution two-photon imaging of the PVSs as they were filled with CSF tracer. In the imaged segments around the pial arteries, the average PVS width was 23.6 ± 2.4 μm before stimulation (Fig. 3a,b). As the artery dilates during hyperemia, the width of the PVS decreases by −1.5 ± 0.6 μm (corresponding to −5.9 ± 2%) (Fig. 3c,d), demonstrating that the change in artery radius directly affects the PVS width, consistent with a recent report in head-fixed awake and naturally sleeping mice[20]. In parallel with the arterial dilation,

a small outward movement of the outer membrane of the PVS of approximately 1 μm was noted (Fig. 3e).

**CSF tracers move from arterial-to-venous PVS**
The glymphatic model describes that CSF flows into the brain along the PVSs surrounding penetrating arteries, disperses through the parenchyma and re-enters the PVSs on the venous side[14,21]. To critically test this model, we injected a CSF tracer into the cisterna magna of NG2-dsRed mice. In these reporter mice, vascular smooth muscle cells express dsRed, allowing the identification of arteries and veins. After 30 or 120 min of CSF tracer circulation, the mice were perfusion-fixed with 4% paraformaldehyde (PFA), their brains were collected and the distribution of tracers along arteries versus veins was blindly scored (Fig. 3f and Extended Data Fig. 4a,b). At 30 min, the tracer was mostly located in the arterial PVSs, but at 120 min, a substantially smaller fraction of arteries exhibited the tracer, while a larger fraction of veins was surrounded by the tracer (Fig. 3g–j and Extended Data Fig. 4c–f). These observations support the idea that CSF inflow occurs along arteries whereas ISF collects along veins for glymphatic export (Extended Data Fig. 4g).

**Functional hyperemia does not drive CSF flow in awake mice**
The experiments reported so far were all performed in mice under KX anesthesia because glymphatic inflow is strongly suppressed by wakefulness[22,23]. However, sensory stimulation induces hemodynamic responses of larger amplitude and shorter temporal profile in awake rodents than during anesthesia[24,25]. In awake mice trained to tolerate head fixation, we tested if functional hyperemia can drive CSF flow
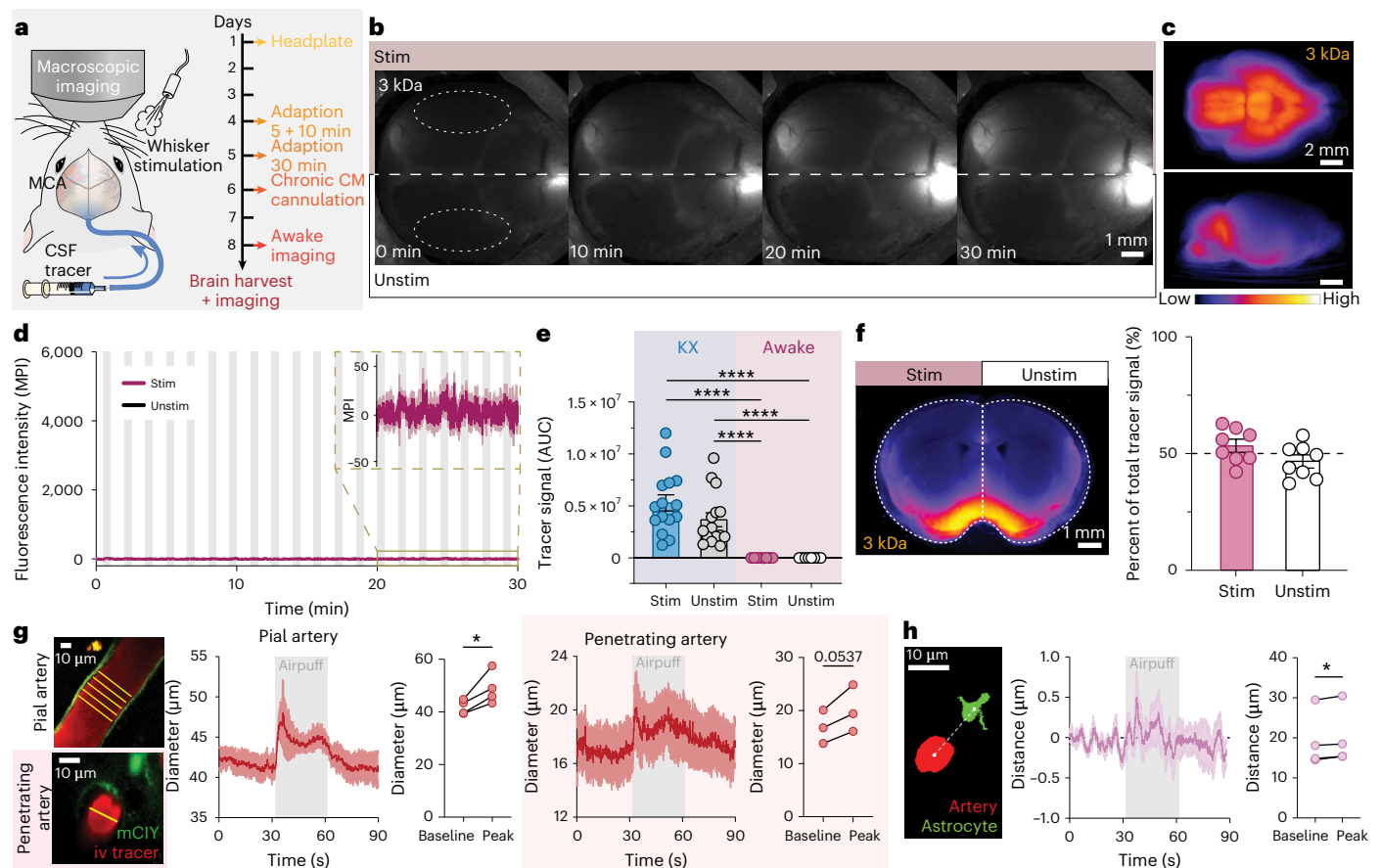
**Fig. 4 | Functional hyperemia does not increase glymphatic influx during wakefulness. a**, Adult wild-type mice were head-plated and chronically implanted with a cannula in the cisterna magna. Mice were adapted to awake head fixation before injection of CSF tracer (3 kDa dextran) and exposure to unilateral whisker stimulation during awake two-photon imaging. **b**, Representative images of tracer influx in awake mice during unilateral whisker stimulation (5 Hz with 10 ms pulses, 20 psi for 30 s with 60 s intervals; dashed circles–ROIs above the middle cerebral artery (MCA)). **c**, Tracer distribution in the whole brain after the ended experiment. Images are overlaid for the entire group. Top, ventral side; bottom, lateral side receiving whisker stimulation ($n = 6$). **d**, Tracer signal (mean pixel intensity) in the stimulated and unstimulated hemisphere in response to whisker stimulations. Gray bars, 30 s whisker stimulation. Inset–zoom of tracer intensity between 20 min and 30 min. **E**, Comparison of tracer influx (area under the curve) between awake ($n = 8$; Fig. 4d) and anesthetized mice ($n = 10$; Fig. 1e). Two-way ANOVA w Tukey's correction, $P < 0.0001$. **f**, Left–ex vivo analysis of the parenchymal tracer distribution of brain tissue sections spanning the barrel

cortex region. Tracer distribution overlaid for the whole group ($n = 8$). Dashed lines, analyzed regions. Right–the percentage distribution of tracer into each hemisphere ($53.4 \pm 2.8\%$ vs. $46.6 \pm 2.8\%$; $n = 8$, eight brain sections/mouse). Two-tailed paired $t$-test, $P = 0.27$. **g**, Mice were injected with a yellow fluorescent protein (YFP)-based chloride sensor expressed in the astrocytic cytosol 2 weeks before insertion of a chronic cranial window. Mice were injected with an i.v. tracer (70 kDa dextran) and exposed to unilateral whisker stimulation during awake two-photon imaging. Representative images of a pial and penetrating segment of the MCA and the corresponding ROIs (yellow) used for diameter analysis. Diameter change of pial (white background, $n = 4$) and penetrating (pink background, $n = 3$) segments of the MCA in awake mice during whisker stimulation. Two-tailed paired $t$-test, $P = 0.034$, pial; $P = 0.054$, penetrating. **h**, Distance between the penetrating artery and surrounding astrocytes during whisker stimulation in wakefulness ($n = 4$). Two-tailed paired $t$-test, $P = 0.0161$. Data are represented as mean $\pm$ s.e.m. *$P < 0.05$ and ****$P < 0.0001$. See also Extended Data Fig. 5a.

during wakefulness (Fig. 4a). After injection, the fluorescent tracer reached the olfactory bulb by spreading along the ventral side of the brain, confirming that the tracer was successfully injected into cisterna magna. However, the tracer did not reach the PVSs around the MCA (Fig. 4b,c). This observation is consistent with earlier studies showing that the glymphatic system is primarily active during sleep or anesthetic regiments that support non-rapid eye movement sleep (NREM) slow wave activity[26]. We next tested if whisker stimulation could overcome the inhibition of perivascular flow during wakefulness. However, 20 periods of whisker stimulation (30-s stimulations intersected by 60-s intervals) failed to drive the CSF tracer into the PVSs surrounding the MCA (Fig. 4b,d). This becomes particularly evident when comparing the tracer signal to that of our anesthetized cohort from Fig. 1e (Fig. 4e and Extended Data Fig. 5a).

To assess CSF tracer influx with high sensitivity, we collected the brains immediately after the stimulation period (30 min) and analyzed

tracer distribution ex vivo. The quantitative image analysis showed no or very little tracer in the cortex surrounding the MCA with no significant difference between the stimulated and unstimulated hemisphere (Fig. 4f). Compared with the anesthetized mice, little parenchymal spread was observed in awake mice (Extended Data Fig. 5b) consistent with previous reports[22,23].

To ensure that the lack of tracer inflow during wakefulness was not caused by an unresponsive arterial wall, we employed two-photon imaging through cranial windows. The analysis showed that both the pial and penetrating segments of the MCA dilated in response to whisker stimulation in awake mice ($8.4 \pm 2.1$ μm and $3.7 \pm 0.7$ μm change, respectively; Fig. 4g). Thus, wakefulness does not support CSF influx along the PVSs of the MCA[22].

A recent study showed that the surrounding tissue moves approximately 1 μm during spontaneous vasomotion in wakefulness[27]. In our dataset, we applied a centroid analysis to measure the distance
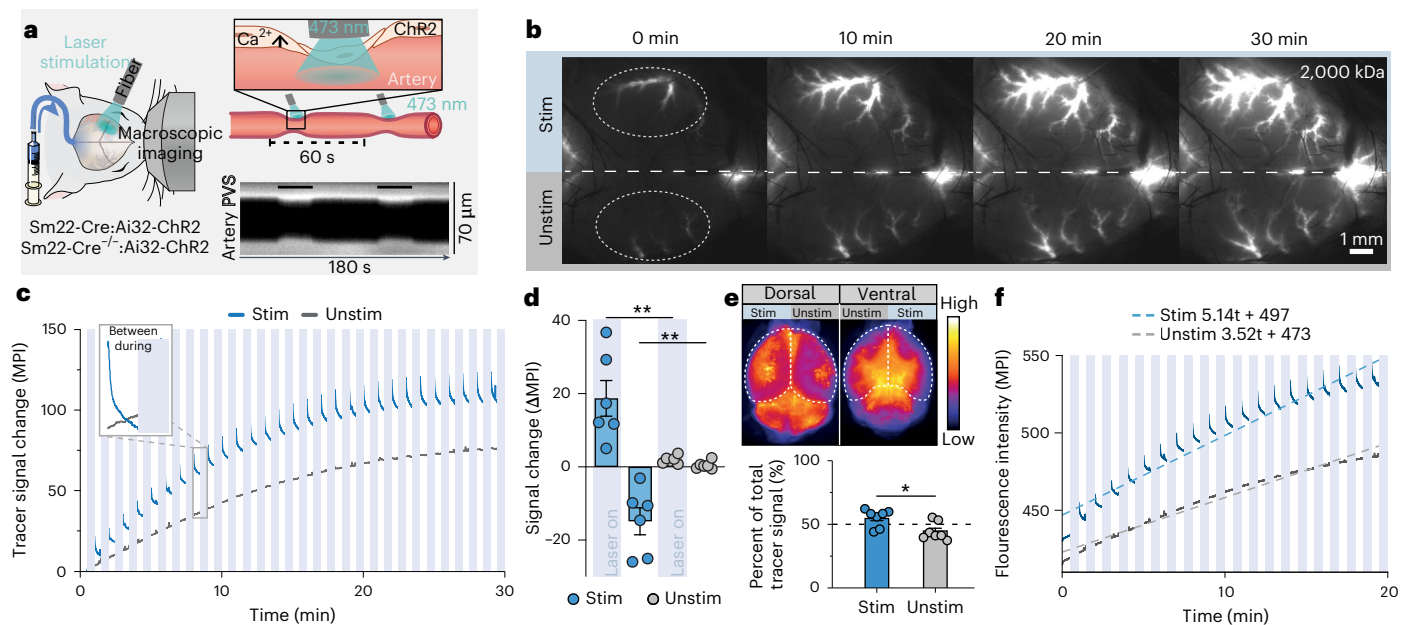
**Fig. 5 | Arterial diameter changes and not neuronal activation per se increases glymphatic influx. a**, We developed an optogenetic mouse line (Sm22-Cre:Ai32-ChR2), where photoactivation of ChR2 in smooth muscle cells leads to arterial constriction. Adult mice were head-plated under KX anesthesia and intracisternally injected with a CSF tracer (2,000 kDa, fluorescein isothiocyanate (FITC)) before exposure to unilateral optogenetic stimulation (473 nm, 10 Hz, 50 ms; 30 s every minute) during macroscopic imaging. Control mice have no expression of channelrhodopsin-2 (Sm22-Cre$^{-/-}$:Ai32-ChR2). Right—light stimulation increases intracellular Ca$^{2+}$ in the smooth muscle cells causing depolarization and vasoconstriction. Bottom—representative kymograph of arterial constriction across two optogenetic stimulations (black bars, 30 s optogenetic stimulation). **b**, Representative images of CSF tracer influx during 30 min circulation. Optogenetic stimulations were given on one hemisphere (stim) every minute for 30 s (10 Hz, 50 ms). **c**, Average change in fluorescent tracer signal (MPI) across 30 min of glymphatic influx with optogenetic stimulations (blue bars; $n = 6$). Mean trace. **d**, Average signal change during and between stimulations ($n = 6$ mice). Two-way ANOVA w Sidak correction, $P = 0.005$ (laser on) and $P = 0.009$ (laser off). **e**, Top—overlay of dorsal and ventral whole-brain images from optogenetic mice. Bottom—percentage distribution of the tracer in the two hemispheres ($55 \pm 2\%$ vs. $45 \pm 2\%$; $n = 7$ mice). Two-tailed paired $t$-test, $P = 0.046$. **f**, Linear fit to the first 20 min of inflow from Fig. 5c, where tracer influx dominates relative to clearance. The linear fits are used to estimate CSF flow rates in the perivascular space based on the tracer signal changes. Data are represented as mean ± s.e.m. *$P < 0.05$ and **$P < 0.01$. See also Fig. Extended Data Fig. 6 and Supplementary Video 3.

between the penetrating artery and surrounding astrocytes. In accordance with the previous findings, we observed a radial displacement of $0.8 \pm 0.1\,\mu$m in response to whisker stimulation in wakefulness supporting the notion that the increase in vascular volume during functional hyperemia is not only linked to changes in the PVS but also triggers a displacement of the surrounding tissue (Fig. 4h).

## Optogenetically induced vasoconstriction increases CSF influx

To test the importance of vascular motion as a driver of CSF influx in anesthetized mice, we used transgenic mice expressing channelrhodopsin-2 (ChR2) in vascular smooth muscle cells (Sm22-Cre:Ai32-ChR2)[28,29]. ChR2-gated cation channels drive an increase in cytosolic Ca$^{2+}$ along with membrane depolarization, which induces arterial constriction[30,31], unlike whisker stimulation that induces dilation. After intracisternal injection of the CSF tracer, we induced repeated vasoconstrictions of the MCA by transcranial optogenetic stimulation of the arterial trunk (30 s stimulation periods every 60 s; Fig. 5a). The optogenetic stimulation did not allow simultaneous tracer recording, so imaging was restricted to intervals between stimulations. Over the course of the experiment, the tracer signal in the PVS of the MCA exposed to optogenetic stimulation increased compared to the unstimulated hemisphere (Fig. 5b,c and Extended Data Fig. 6a,b; Supplementary Video 3). By subtracting the MPI before and after stimulations, we found that each individual stimulation caused the tracer signal to increase in the stimulated hemisphere ($9.1 \pm 2.4\,\Delta$MPI; Fig. 5d). Between stimulations, as the artery dilated, the signal decreased ($-6.6 \pm 1.7\,\Delta$MPI). In the unstimulated hemisphere, there was no change

in tracer signal during or between stimulations. In Cre-negative control animals (Sm22-Cre$^{-/-}$:Ai32-ChR2), glymphatic influx was unaffected by optogenetic stimulation (Extended Data Fig. 6c). These observations suggest that it is not the neuronal activity per se that drives perivascular CSF influx, but rather the dynamic changes in arterial diameter. Furthermore, the observations point to the conclusion that it is not specifically the positive (dilation) or negative (constriction) change in diameter but rather vasomotion that propels CSF flow along the PVSs.

Analysis of the parenchymal tracer distribution in ex vivo vibratome slices from optogenetic mice revealed that laser-induced vasoconstriction increases tracer accumulation in the stimulated hemisphere (Fig. 5e), similar to the tracer accumulation driven by whisker stimulation-induced vasomotion (Fig. 1k). In conclusion, both sensory stimulation and artificial manipulation of the arterial diameter result in an increased CSF flow and influx of CSF tracer into the neuropil in the stimulated hemisphere, supporting the concept that dynamic changes in arterial diameter is a direct driver of glymphatic inflow.

## CSF flow rate estimates are higher in the stimulated hemisphere

Based on our two-photon and macroscopic imaging, we next estimated the CSF volume flow rate in the PVS in response to vascular changes. First, we estimated the CSF flow rate during baseline flow without stimulations, which led to a CSF flow rate estimate of $2.2 \times 10^5\,\mu$m$^3$ s$^{-1}$. Next, to estimate the CSF flow rate in the stimulated hemisphere during whisker-stimulation experiments, we reasoned that it must be proportional to the flow rate in the unstimulated hemisphere, with a proportionality constant equal to the ratio of the rates of change of their MPIs
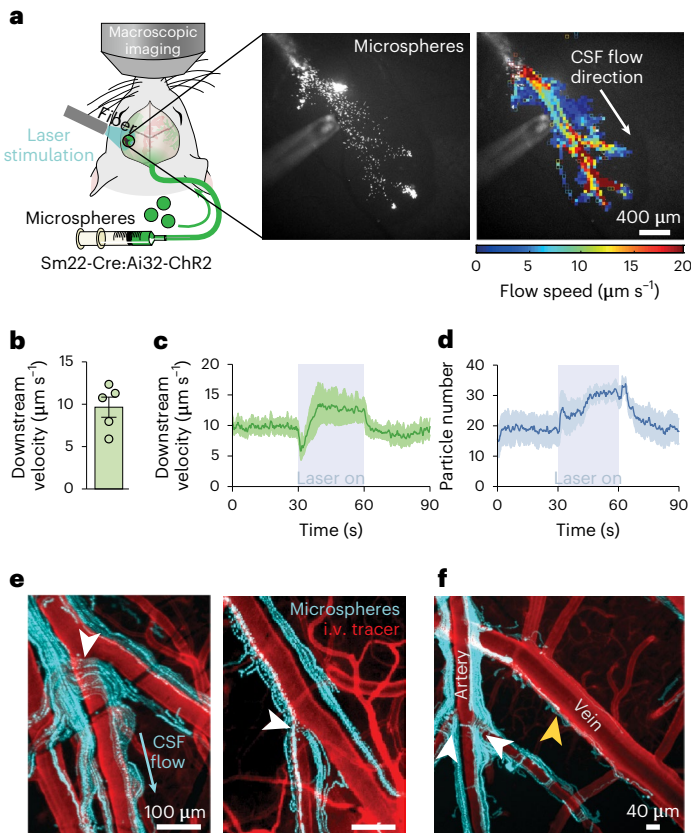
**Fig. 6 | Laser stimulation in optogenetic mice increases CSF downstream velocity. a**, Left—we developed an optogenetic mouse line (Sm22-Cre:Ai32-ChR2), where photoactivation of ChR2 in smooth muscle cells leads to arterial constriction. Adult mice were head-plated, and a cranial window was inserted above the middle cerebral artery under KX anesthesia. Microspheres (1 μm) were injected into the cisterna magna before exposure to unilateral optogenetic stimulation (473 nm, 10 Hz, 50 ms; 30 s with 60 s interval) during macroscopic imaging. Middle—microspheres are traveling in the perivascular space. The laser fiber was aimed at the middle cerebral artery segment. Right—particle tracking flowmetry was applied to calculate the mean flow speed of microspheres in the perivascular space. **b**, The average downstream CSF flow velocity between $t = 0$–30 s ($n = 5$). **c**, Average CSF flow velocity of microspheres in response to optogenetic stimulation ($n = 5$ mice). **d**, Average particle number within the arterial segment in response to optogenetic stimulation ($n = 5$ mice). **e**, Representative images of 1 μm microspheres moving around pial arterial branches at branching points (white arrowheads, $n = 5$). The image is a 30-s maximum projection showing the microsphere trajectories before any whisker stimulations. The blue arrow indicates the direction of the CSF flow, which is parallel to the blood flow. **f**, As the laser stimulation ceases, the arterial dilation pushes particles from the pial arterial to venous perivascular spaces (yellow arrowhead, $n = 3$). Data are represented as mean ± s.e.m.

(Methods). Determining those rates of change via linear fits to the tracer signals in both hemispheres (Fig. 1e), we were able to estimate a CSF inflow rate of $3.6 \times 10^5$ μm³ s⁻¹ in the stimulated hemisphere (Fig. 1l), 1.6 times faster than baseline CSF flow. For the optogenetically stimulated mice, we assumed the same baseline inflow rate in the unstimulated hemisphere and estimated the inflow rate in the stimulated hemisphere by similar linear fits (Fig. 5f), finding the rate to be $3.3 \times 10^5$ μm³ s⁻¹. These calculations provide the first quantitative estimate of glymphatic CSF influx in the cortical region supplied by the MCA.

## Vasoconstriction increases downstream CSF flow velocity

To understand how vasoconstriction affects perivascular CSF flow, we next used macroscopic imaging to map the movement of microspheres over a larger area, again using particle tracking velocimetry (PTV) to obtain quantitative measures of perivascular CSF flow (Fig. 6a). Before stimulation, the CSF flow velocity was $9.7 \pm 1.2$ μm s⁻¹ ($t = 0$–30 s; Fig. 6b), which is lower but within the range of our previously measured CSF flow velocity (Fig. 2c). As particles travel in the PVSs, some get stuck on the PVS wall. In our PTV analysis, we attempt to exclude these particles, but in the large field of view (FOV) of a macroscope, there will be more microspheres that do not move included in the analysis compared to the two-photon imaging (Fig. 2), which likely explains the low CSF flow velocity. The vasoconstriction initially caused a transient decrease in CSF flow velocity to $5.1 \pm 1.1$ μm s⁻¹, likely a consequence of distal microspheres being pulled toward the stimulation site, where vasoconstriction transiently increases the PVS volume (Fig. 6c). However, the CSF flow velocity quickly increased, and the overall effect of vasoconstriction was thus an increase in CSF flow velocity ($12 \pm 2.4$ μm s⁻¹ between $t = 30$–60 s). In parallel, the number of particles increased during the stimulation period (Fig. 6d). This demonstrates that vasoconstriction induced by optogenetic stimulation increases the CSF flow in the pial MCA, which supports our previous findings of higher glymphatic influx and clearance in response to dynamic changes of arterial diameter.

## Microspheres move around arterial segments at bifurcations

Furthermore, we made two minor but interesting observations based on the analysis of microsphere transport following optogenetic stimulation of smooth muscle cells. We observed that at bifurcations, microspheres can move around the artery to reach the PVSs inside the branching point (Fig. 6e). The two-dimensional (2D) imaging does not resolve whether they move above or below. This suggests that there are small PVS tracts around bifurcations that facilitate CSF flow into higher-order branches of the PVS system. First, we observe this phenomenon in the pial PVSs, where the PVSs take a triangular shape that optimizes CSF flow[32,33]. Secondly, we observe that microspheres can cross from arterial to venous PVSs as the artery dilates after cessation of laser stimulation (at $t = 60$ s; Fig. 6f). We speculate that the vasodilation increases the pressure in the PVS, suggesting that the arterial-to-venous PVS route is a high-resistance pathway, at least compared to the arterial perivascular compartment. This occurs in the pial PVSs, where arteries and veins cross. It is also worth noting that it was only a fraction of microspheres that crossed over to the venous segments because the majority remained in the arterial PVSs.

## Whisker stimulation increases glymphatic clearance

All cellular activity produces metabolic waste, so we hypothesized that glymphatic flow is increased along with blood flow during functional hyperemia to boost clearance. To test this idea, we allowed the CSF tracer to circulate for 30 min to saturate the PVSs of the MCA before stimulating the whiskers repeatedly (30 s per stimulation) during 30 min of imaging through the intact skull (totaling 20 stimulations per mouse; Fig. 7a). We found that repeated whisker stimulation causes faster clearance of tracer from the stimulated hemisphere (Fig. 7b–d). In the unstimulated hemisphere, clearance was slower and the total tracer removal was less. Thus, this analysis demonstrates that functional hyperemia causes a faster removal of CSF tracer from the PVSs.

## Impedance pumping models reproduce flow characteristics

We speculated which fluid dynamical mechanism might explain the flow characteristics observed in vivo, particularly the counterintuitive fact that CSF influx is increased both by vasodilation and by vasoconstriction or opposite motions. We found that impedance pumping models reproduce our observations, including the fact that microspheres are transiently pulled toward the site of vasoconstriction. Impedance pumping can occur when a fluid-filled vessel with flexible walls, such as a PVS, is subjected to active, repeating dilation and/or constriction in a local region[34,35], such as in the embryonic heart, where impedance pumping is important for unidirectional forward flow[36]. Those motions

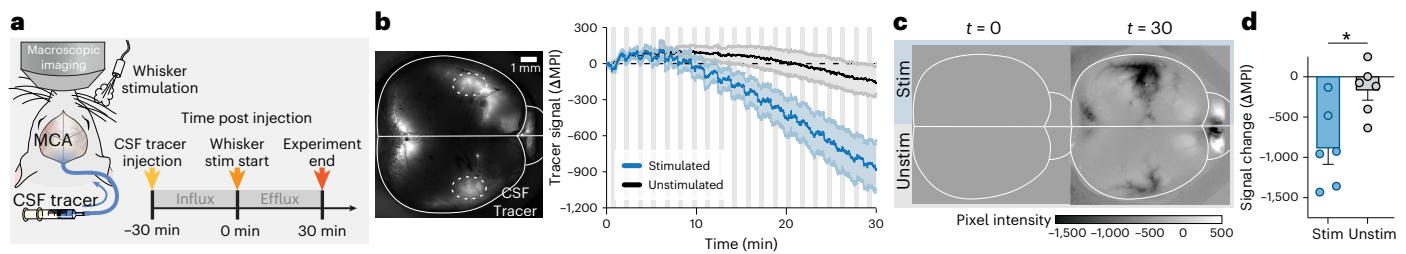**Fig. 7 | Functional hyperemia increases glymphatic clearance. a**, Adult wild-type mice were head-plated under KX anesthesia. CSF tracer (3 kDa dextran) was injected into the cisterna magna and circulated for 30 min before exposure to unilateral whisker stimulation during macroscopic imaging. **b**, Left–representative image of CSF tracer in the perivascular spaces along the middle cerebral artery. ROIs are outlined by dotted circles. Right–change in tracer signal (MPI) in the middle cerebral artery area across 30 min of unilateral whisker stimulation ($n = 6$). **c**, The change in tracer signal from $t = 0$ to $t = 30$ min. Dark pixels denote less tracer signal. The representative image was averaged across 20 frames (4 s) to improve resolution. **d**, Quantification of the total change in mean pixel intensity for each hemisphere across the 30 min ($n = 6$). Two-tailed paired $t$-test, $P = 0.037$. Data are represented as mean ± s.e.m. *$P < 0.05$.

displace fluid locally while also propagating in both directions along elastic vessel walls as waves, which eventually encounter wall features that cause partial or total wave reflection, such as bifurcations, connections to a different fluid chamber or sudden changes in wall stiffness, density or diameter. Primary and reflected waves then interfere constructively or destructively, and if their interference causes a net flow, impedance pumping is said to occur. The flow speed and direction (downstream or upstream) are determined primarily by the wave speed, locations of reflectors and repetition frequency. Flow direction is not strongly affected by changing dilation to constriction.

We built numerical models of impedance pumping in a simplified PVS (Methods). First, we modeled functional hyperemia induced by whisker stimulation. To do so, we drove periodic dilation of the artery wall near the left side of a simulation domain by applying a periodic force there (Fig. 8a,c). Dilation caused pulsatile CSF flow in the surrounding PVS (Fig. 8b,d and Supplementary Video 4). At a cross-section near the left end of the PVS domain, flow proceeded primarily to the left during dilation and to the right when the artery diameter was unperturbed. The flow, however, was not entirely symmetric, and simulated flow tracers moved to the right over time (Fig. 8e). Similarly, the net flux (normalized cumulative volume of CSF moving to the right through the same cross-section) oscillated with each dilation cycle but increased steadily over long times (Fig. 8f).

Next, we modeled vasoconstriction caused by optogenetic stimulation. To do so, we drove periodic constriction of the artery wall (Fig. 8g,i and Supplementary Video 5). Constriction, like dilation, caused alternating flow in the surrounding PVS, but with opposite direction–at the same cross-section, flow proceeded primarily to the right during constriction and to the left when the artery diameter was unperturbed (Fig. 8h,j). Nonetheless, tracers again moved to the right over time, and the net flux of CSF again increased steadily (Fig. 8k,l). Other proposed models include a poroelastic model, where temporal asymmetry in arterial pulsation and nonlinear response of brain tissue are combined[17]. Future studies should explore whether poroelastic and impedance pumping act in concert to orchestrate the unidirectional CSF flow in the periarterial space.

## Discussion

Our study demonstrates that functional hyperemia accelerates perivascular CSF influx. The increased CSF transport is not only noticeable for glymphatic influx but also causes faster *clearance* of CSF tracer in response to whisker stimulation. Using optogenetics, we demonstrate that it is not neuronal activation that directly increases CSF influx, but rather the changes in arterial diameter, which, during physiological conditions, are driven by neural activation. We use a simple numerical model to show that impedance pumping may be the fluid dynamical mechanism by which these arterial diameter changes can drive CSF

regardless of whether they are constrictions or dilations. Our experimental paradigm consists of many stimulations delivered in sequence, which suggests that a dynamic vasculature is important for driving CSF flow. Because functional hyperemia is also induced by visual, auditory and tactile stimulation[37–40], as well as spontaneous neuronal activity[41,42], we predict that vasomotion will drive CSF inflow in a similar manner independent of what initiates the neural activity.

Human magnetic resonance imaging (MRI) studies have shown that neural and hemodynamic slow oscillations are interlinked with CSF flow in the fourth ventricle during sleep[3]. During sleep, neural activations rhythmically move through the brain and are coupled to increases in blood flow[43–45]. Large fluctuations in cerebral blood volume and arterial diameter changes have also been observed in response to oscillatory changes in norepinephrine[46,47]. We here studied the interrelationship between vascular dynamics and CSF transport in KX-anesthetized mice. The advantage of rodent studies is that it is possible to obtain kinetic data on CSF flow in the periarterial spaces with high spatial and temporal resolution. This analysis demonstrated that functional hyperemia on a local scale can enhance CSF inflow and glymphatic clearance. The findings reported here might provide insight into how resting state activity during sleep drives CSF flow in the PVSs. In future experiments, it will be interesting to measure CSF flow and vascular diameter during natural sleep to test the capacity of spontaneous diameter changes to drive CSF flow during NREM sleep. It was not possible here, due to the arousing effects of whisker stimulation. Noninvasive MRI measurements of fluid dispersion, such as spin labeling and magnetic resonance encephalography (MREG), are in the future expected to address the effect of the sleep-wake cycle on brain fluid transport.

In awake head-fixed mice, both spontaneous and visually evoked vasomotions have been shown to drive clearance[37]. Our minimally invasive experimental setup is based on transport along the PVSs surrounding the MCAs; however, wakefulness potently suppresses glymphatic activity due to the high level of norepinephrine and a decrease in the extracellular space volume[22]. Thus, it was not possible here to study glymphatic influx or efflux in awake mice. It is important to note that the lack of CSF periarterial inflow in awake mice exposed to whisker stimulation is not a consequence of the suppression of functional hyperemia–During wakefulness, the hemodynamic response of functional hyperemia is faster and of larger amplitude than during anesthesia[24,48] (Fig. 4g). As discussed, shrinkage of the extracellular space volume is known to contribute to the suppression of glymphatic flow in wakefulness, but other mechanisms are likely to be in play.

Several studies have argued that physiological CSF flow is driven by artery wall pulsations advancing in the blood flow direction[18,49,50]. However, dilations due to natural functional hyperemia propagate opposite of blood flow[1]. Our optogenetic constrictions were triggered
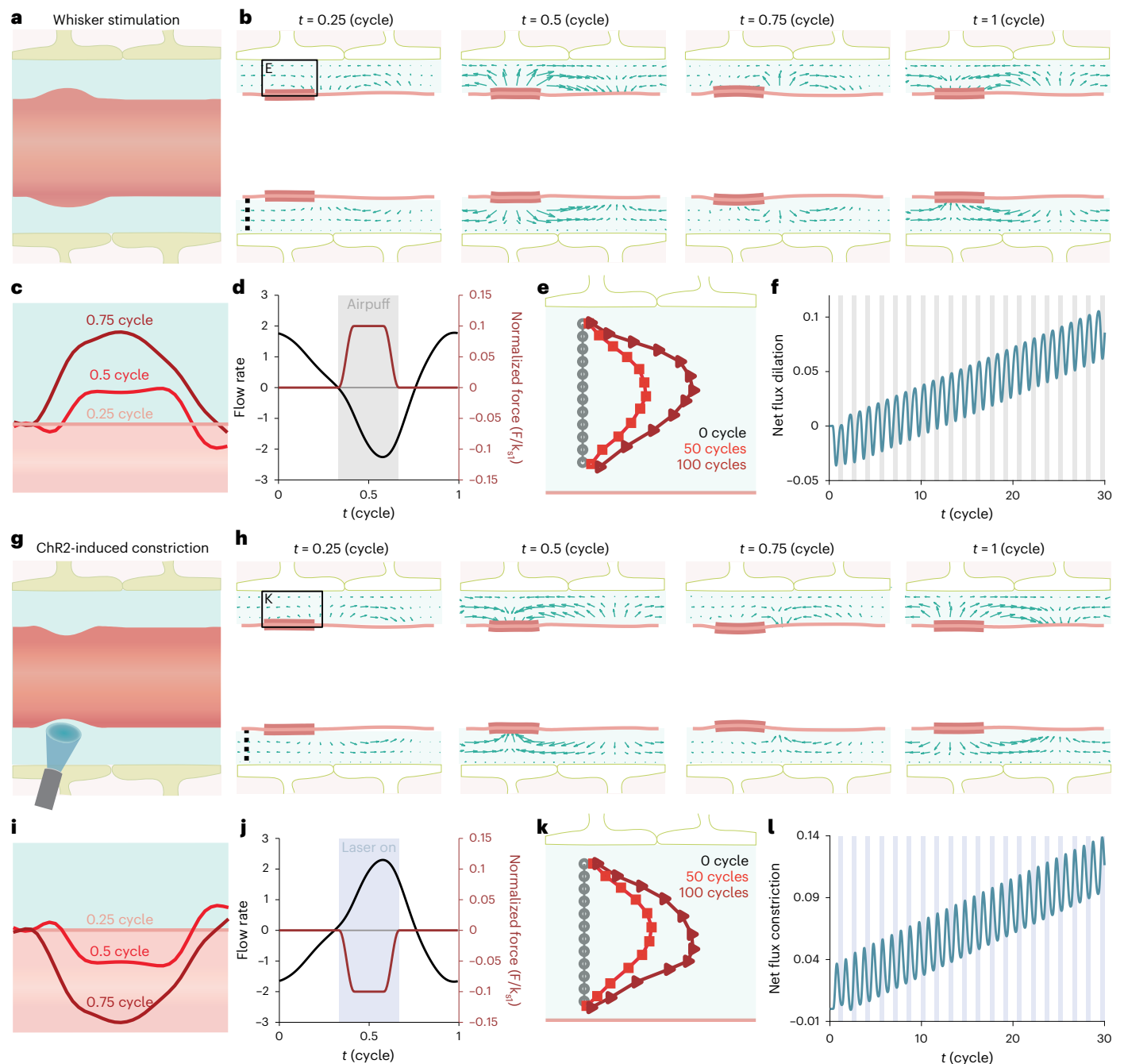
**Fig. 8 | Impedance pumping models reproduce characteristics of flows driven by functional hyperemia and optogenetic stimulation. a**, The first model is based on arterial dilation, which we experimentally induced by unilateral whisker stimulation. **b**, In the first model, an arteriolar wall (red, shown in cross-section) actively dilates and relaxes in a small region (shaded red), with wall motion spreading in both directions along the artery, causing the flow of CSF (arrows) in the surrounding perivascular spaces. **c**, Local wall motion across one dilatory cycle (enlargement of red shaded area in B). **d**, The volume flow rate through one cross-section of the perivascular space (dashed line in B) varies over each dilation cycle. Flow is decreased during local dilation, with a slight lag, and increases during local relaxation. **e**, Over many cycles, the flow carries passive tracers to the right along the perivascular space (enlargement of region marked in B).

**f**, The net flux (cumulative volume of fluid moving rightward through the cross-section shown in B) oscillates and increases steadily over time. Gray bars, whisker stimulations. **g**, The second model is based on local vasoconstriction, which experimentally is obtained by optogenetic stimulation of mice expressing ChR2 in smooth muscle cells. **h,i**, In our second model, the artery constricts instead of dilating, driving a flow with different spatial structures and different volume flow rates. **j–l**, In the constriction model, as in the dilation model, tracer moves to the right and net flux increases over time. The direction of the tracer (to the right, not left) is determined by the location of the active arterial diameter change, not by whether it is dilation or constriction. Blue bars, laser stimulations. See also Extended Data Fig. 7 and Supplementary Videos 4 and 5.

by focal laser stimulation, so neither of the prior models applies here. An alternate model is impedance pumping, in which local dilations and/or constrictions cause waves that propagate passively, both upstream and downstream, reflect, and through wave interference,

drive a net flow[34,35]. Strong pulsations were accompanied by a net flow that moved fluid and tracers in one direction over long times, consistent with the observations that functional hyperemia enhances solute clearance (Fig. 7b). It is important to note that the impedance

pumping models are far simpler than the physiological systems and cannot yet make precise, quantitative flow predictions. The simulation domains are 2D, and all quantities are unitless. Still, impedance pumping produces pulsatile, directional flow and is known to occur biologically in the embryonic heart that uses impedance pumping to drive unidirectional forward flow[36].

Altogether, the observations reported here show that arterial diameter changes induced by whisker stimulation increase CSF inflow and enhance glymphatic clearance. We show that arterial diameter fluctuations are an important driver of glymphatic activity, by optogenetically bypassing neural activation and directly triggering arterial diameter changes. Under normal physiological conditions, neural activity also regulates extracellular space geometry and diffusibility, which also may contribute to the regulation of CSF flow in the PVSs[51]. In aging, the activity of the glymphatic system declines[52,53], possibly because neurovascular coupling decreases[54]. The decrease in vascular elasticity in aging may mechanistically link the reduction of both functional hyperemia and periarterial CSF influx[55,56]. Interestingly, it has recently been shown that macrophages located in the leptomeningeal membranes—including Slym—and PVSs are strategically located to facilitate the breakdown of large proteins[57,58], which otherwise exhibit very slow clearance[7], to enable subsequent clearance of smaller fragments out of the brain. Additionally, the macrophages facilitate CSF flow through extracellular matrix remodeling, which in turn affects arterial stiffness[58]. Thus, we propose that maintaining a healthy cerebral vasculature not only preserves the delivery of energy metabolites to active brain regions but also drives glymphatic efflux and thereby protects against age-related proteinopathies.

## Online content

Any methods, additional references, Nature Portfolio reporting summaries, source data, extended data, supplementary information, acknowledgements, peer review information; details of author contributions and competing interests; and statements of data and code availability are available at https://doi.org/10.1038/s41593-023-01327-2.

## References

1. Rungta, R. L., Chaigneau, E., Osmanski, B.-F. & Charpak, S. Vascular compartmentalization of functional hyperemia from the synapse to the pia. *Neuron* **99**, 362–375 (2018).
2. Drew, P. J. Neurovascular coupling: motive unknown. *Trends Neurosci.* **45**, 809–819 (2022).
3. Fultz, N. E. et al. Coupled electrophysiological, hemodynamic, and cerebrospinal fluid oscillations in human sleep. *Science* **366**, 628–631 (2019).
4. Takano, T. et al. Astrocyte-mediated control of cerebral blood flow. *Nat. Neurosci.* **9**, 260–267 (2006).
5. Wang, X. et al. Astrocytic Ca$^{2+}$ signaling evoked by sensory stimulation in vivo. *Nat. Neurosci.* **9**, 816–823 (2006).
6. Takata, N. et al. Cerebral blood flow modulation by basal forebrain or whisker stimulation can occur independently of large cytosolic Ca$^{2+}$ signaling in astrocytes. *PLoS One* **8**, e66525 (2013).
7. Plá, V. et al. A real-time in vivo clearance assay for quantification of glymphatic efflux. *Cell Rep.* **40**, 111320 (2022).
8. Dana, H. et al. Thy1-GCaMP6 transgenic mice for neuronal population imaging in vivo. *PLoS One* **9**, e108697 (2014).
9. Ma, Y. et al. Wide-field optical mapping of neural activity and brain haemodynamics: considerations and novel approaches. *Philos. Trans. R. Soc. B Biol. Sci.* **371**, 20150360 (2016).
10. Ding, F. et al. α1-Adrenergic receptors mediate coordinated Ca$^{2+}$ signaling of cortical astrocytes in awake, behaving mice. *Cell Calcium* **54**, 387–394 (2013).
11. Wang, X., Takano, T. & Nedergaard, M. Astrocytic calcium signaling: mechanism and implications for functional brain imaging. *Methods Mol. Biol.* **489**, 93–109 (2009).
12. Schulz, K. et al. Simultaneous BOLD fMRI and fiber-optic calcium recording in rat neocortex. *Nat. Methods* **9**, 597–602 (2012).
13. Ma, Y. et al. Resting-state hemodynamics are spatiotemporally coupled to synchronized and symmetric neural activity in excitatory neurons. *Proc. Natl Acad. Sci. USA* **113**, E8463–E8471 (2016).
14. Iliff, J. J. et al. A paravascular pathway facilitates CSF flow through the brain parenchyma and the clearance of interstitial solutes, including amyloid. *Sci. Transl. Med.* **4**, 147ra111 (2012).
15. Plog, B. A. et al. Transcranial optical imaging reveals a pathway for optimizing the delivery of immunotherapeutics to the brain. *JCI Insight* **3**, 2–3 (2018).
16. Bohr, T. et al. The glymphatic system: current understanding and modeling. *iScience* **25**, 104987 (2022).
17. Kedarasetti, R. T., Drew, P. J. & Costanzo, F. Arterial vasodilation drives convective fluid flow in the brain: a poroelastic model. *Fluids Barriers CNS* **19**, 34 (2022).
18. Mestre, H. et al. Flow of cerebrospinal fluid is driven by arterial pulsations and is reduced in hypertension. *Nat. Commun.* **9**, 4878 (2018).
19. Bedussi, B., Almasian, M., de Vos, J., VanBavel, E. & Bakker, E. N. T. P. Paravascular spaces at the brain surface: low resistance pathways for cerebrospinal fluid flow. *J. Cereb. Blood Flow. Metab.* **38**, 719–726 (2018).
20. Bojarskaite, L. et al. Sleep cycle-dependent vascular dynamics in male mice and the predicted effects on perivascular cerebrospinal fluid flow and solute transport. *Nat. Commun.* **14**, 953 (2023).
21. Iliff, J. J. et al. Brain-wide pathway for waste clearance captured by contrast-enhanced MRI. *J. Clin. Invest.* **123**, 1299–1309 (2013).
22. Xie, L. et al. Sleep drives metabolite clearance from the adult brain. *Science* **342**, 373–377 (2013).
23. von Holstein-Rathlou, S., Petersen, N. C. & Nedergaard, M. Voluntary running enhances glymphatic influx in awake behaving, young mice. *Neurosci. Lett.* **662**, 253–258 (2018).
24. Martin, C., Martindale, J., Berwick, J. & Mayhew, J. Investigating neural–hemodynamic coupling and the hemodynamic response function in the awake rat. *Neuroimage* **32**, 33–48 (2006).
25. Gao, Y.-R. et al. Time to wake up: studying neurovascular coupling and brain-wide circuit function in the un-anesthetized animal. *Neuroimage* **153**, 382–398 (2017).
26. Hablitz, L. M. et al. Increased glymphatic influx is correlated with high EEG delta power and low heart rate in mice under anesthesia. *Sci. Adv.* **5**, eaav5447 (2019).
27. Kedarasetti, R. T. et al. Functional hyperemia drives fluid exchange in the paravascular space. *Fluids Barriers CNS* **17**, 52 (2020).
28. Madisen, L. et al. A toolbox of Cre-dependent optogenetic transgenic mice for light-induced activation and silencing. *Nat. Neurosci.* **15**, 793–802 (2012).
29. Holtwick, R. et al. Smooth muscle-selective deletion of guanylyl cyclase-A prevents the acute but not chronic effects of ANP on blood pressure. *Proc. Natl Acad. Sci. USA* **99**, 7142–7147 (2002).
30. Wu, Y. et al. Optogenetic approach for functional assays of the cardiovascular system by light activation of the vascular smooth muscle. *Vascul. Pharmcol.* **71**, 192–200 (2015).
31. Kim, M., Hong, J., Kim, J. & Shin, H. Fiber bundle-based integrated platform for wide-field fluorescence imaging and patterned optical stimulation for modulation of vasoconstriction in the deep brain of a living animal. *Biomed. Opt. Express* **8**, 2781 (2017).
32. Tithof, J., Kelley, D. H., Mestre, H., Nedergaard, M. & Thomas, J. H. Hydraulic resistance of periarterial spaces in the brain. *Fluids Barriers CNS* **16**, 19 (2019).
33. Vinje, V., Bakker, E. N. T. P. & Rognes, M. E. Brain solute transport is more rapid in periarterial than perivenous spaces. *Sci. Rep.* **11**, 16085 (2021).

34. Hickerson, A. I. & Gharib, M. On the resonance of a pliant tube as a mechanism for valveless pumping. *J. Fluid Mech.* **555**, 141 (2006).

35. Avrahami, I. & Gharib, M. Computational studies of resonance wave pumping in compliant tubes. *J. Fluid Mech.* **608**, 139–160 (2008).

36. Forouhar, A. S. et al. The embryonic vertebrate heart tube is a dynamic suction pump. *Science* **312**, 751–753 (2006).

37. van Veluw, S. J. et al. Vasomotion as a driving force for paravascular clearance in the awake mouse brain. *Neuron* **105**, 549–561 (2020).

38. Sanganahalli, B. G., Bailey, C. J., Herman, P. & Hyder, F. Tactile and non-tactile sensory paradigms for fMRI and neurophysiologic studies in rodents. *Methods Mol. Biol.* **489**, 213–242 (2009).

39. Janik, R. et al. Attenuation of functional hyperemia to visual stimulation in mild Alzheimer's disease and its sensitivity to cholinesterase inhibition. *Biochim. Biophys. Acta* **1862**, 957–965 (2016).

40. Chen, C. et al. Study of neurovascular coupling by using mesoscopic and microscopic imaging. *iScience* **24**, 103176 (2021).

41. Drew, P. J., Winder, A. T. & Zhang, Q. Twitches, blinks, and fidgets: important generators of ongoing neural activity. *Neuroscientist* **25**, 298–313 (2019).

42. Winder, A. T., Echagarruga, C., Zhang, Q. & Drew, P. J. Weak correlations between hemodynamic signals and ongoing neural activity during the resting state. *Nat. Neurosci.* **20**, 1761–1769 (2017).

43. Raichle, M. E. The restless brain. *Brain Connect.* **1**, 3–12 (2011).

44. Huang, J. Greater brain activity during the resting state and the control of activation during the performance of tasks. *Sci. Rep.* **9**, 5027 (2019).

45. Bergel, A., Deffieux, T., Demené, C., Tanter, M. & Cohen, I. Local hippocampal fast gamma rhythms precede brain-wide hyperemic patterns during spontaneous rodent REM sleep. *Nat. Commun.* **9**, 5364 (2018).

46. Turner, K. L., Gheres, K. W., Proctor, E. A. & Drew, P. J. Neurovascular coupling and bilateral connectivity during NREM and REM sleep. *eLife* **9**, e62071 (2020).

47. Kjaerby, C. et al. Memory-enhancing properties of sleep depend on the oscillatory amplitude of norepinephrine. *Nat. Neurosci.* **25**, 1059–1070 (2022).

48. Pisauro, M. A., Dhruv, N. T., Carandini, M. & Benucci, A. Fast hemodynamic responses in the visual cortex of the awake mouse. *J. Neurosci.* **33**, 18343–18351 (2013).

49. Hadaczek, P. et al. The "perivascular pump" driven by arterial pulsation is a powerful mechanism for the distribution of therapeutic molecules within the brain. *Mol. Ther.* **14**, 69–78 (2006).

50. Wang, P. & Olbricht, W. L. Fluid mechanics in the perivascular space. *J. Theor. Biol.* **274**, 52–57 (2011).

51. Chvátal, A. et al. Changes in glial $K^+$ currents with decreased extracellular volume in developing rat white matter. *J. Neurosci. Res.* **49**, 98–106 (1997).

52. Kress, B. T. et al. Impairment of paravascular clearance pathways in the aging brain. *Ann. Neurol.* **76**, 845–861 (2014).

53. da Mesquita, S. et al. Aging-associated deficit in CCR7 is linked to worsened glymphatic function, cognition, neuroinflammation, and β-amyloid pathology. *Sci. Adv.* **7**, 4601–4622 (2021).

54. Toth, P., Tarantini, S., Csiszar, A. & Ungvari, Z. Functional vascular contributions to cognitive impairment and dementia: mechanisms and consequences of cerebral autoregulatory dysfunction, endothelial impairment, and neurovascular uncoupling in aging. *Am. J. Physiol. Heart Circ. Physiol.* **312**, H1–H20 (2017).

55. Lacolley, P., Regnault, V., Segers, P. & Laurent, S. Vascular smooth muscle cells and arterial stiffening: relevance in development, aging, and disease. *Physiol. Rev.* **97**, 1555–1617 (2017).

56. Monk, B. A. & George, S. J. The effect of ageing on vascular smooth muscle cell behaviour—a mini-review. *Gerontology* **61**, 416–426 (2015).

57. Møllgård, K. et al. A mesothelium divides the subarachnoid space into functional compartments. *Science* **379**, 84–88 (2023).

58. Drieu, A. et al. Parenchymal border macrophages regulate the flow dynamics of the cerebrospinal fluid. *Nature* **611**, 585–593 (2022).

## Methods

### Animals

Animal experiments were approved by the Danish Animal Experiments Inspectorate or the University Committee on Animal Resources of the University of Rochester and performed according to guidelines from the National Institutes of Health (NIH). The mice had ad libitum food and water access in an environment with a 12 h light/12 h dark cycle (lights on at 7 a.m.) at 21 °C with 40–60% humidity. We used a mixture of males and females for the studies and, if not otherwise stated, we used C57BL/6JRj (Janvier). For measurement of cerebral blood flow and neuronal activity, we used the GCaMP-expressing strains GLT1-GCaMP7 (ref. [59]; RIKEN BRC, RBRC09650; bred in house) and Thy1-GCaMP6S[8] (Jackson, 024275; bred in house), respectively. The GLT1 promotor is located in both astrocytes and neurons, whereas Thy1 is exclusively located in neurons. For optogenetic experiments, we bred mice expressing ChR2 in smooth muscle cells (Sm22-Cre:Ai32-ChR2, bred in house; Jackson, 024109 and 017491 (refs. [28,29])). Cre-negative littermates were used as controls (Sm22-Cre$^{-/-}$:Ai32-ChR2). To assess CSF tracer around arteries and veins, we used NG2-dsRed mice with fluorescently labeled vascular smooth muscle cells (Jackson, 008241 (ref. [60])).

### Surgery and anesthesia

Mice were anesthetized with a KX mixture (100 mg kg$^{-1}$; 10 mg kg$^{-1}$, i.p.) and fixed in a stereotaxic frame. Lidocaine (2 mg kg$^{-1}$, s.c.) and buprenorphine (0.05 mg kg$^{-1}$, i.p.) were injected for pain management. During surgery, mice were positioned on a heating pad to maintain body temperature at 37 °C. During surgery and subsequent imaging, anesthesia was maintained by alternating ketamine (50 mg kg$^{-1}$, s.c.) and KX (50 mg kg$^{-1}$; 5 mg kg$^{-1}$, s.c.) injections every 30–45 min. When head-fixing was required for imaging, the skin and fascia were cut way to expose the skull and dried with a cotton swap. A head plate was fastened with dental cement. For recovery surgeries, the mice received postoperative analgesia (carprofen, 5 mg kg$^{-1}$, s.c.) at 0, 24 and 48 h.

### In vivo glymphatic imaging

For studies of the glymphatic system, the cisterna magna was exposed and a 30GA needle was inserted. Superglue was used to fix it in place and dental cement to cover the incision (previously detailed[61]). For imaging performed under anesthesia, mice were transferred to a microscope for macroscopic or two-photon imaging (see imaging details further down). Fluorescent CSF tracer (10 μl tetramethylrhodamine (TMR)-labeled 70 kDa dextran, 2.5%; Thermo Fisher Scientific, D1818) was injected at a rate of 2 μl min$^{-1}$ over 5 min[62,63] with a syringe pump (KD Scientific, Legato 130). As the CSF tracer reached the trunk of the MCAs, whisker stimulations were applied for 30 min ($n = 10$, 5 females and 5 males, 13–14 weeks). Control mice received no whisker stimulation ($n = 7$, 5 female, 2 male, 11 weeks).

### Whisker stimulation

Whiskers were stimulated unilaterally by air puffs from a pneumatic pressure pump (Picospritzer, Parker) controlled by a digitizer (Molecular Devices, Axon Digidata 1550B plus HumSilencer), which was programmed via Clampex software (Axon pCLAMP). The whisker stimulations were delivered for 30 s with 60 s interval, and for protocol optimization, we applied frequencies of 1, 5 or 10 Hz and pulse lengths of 5, 10 or 15 ms[11,12]. Air pressure was set between 10 psi and 20 psi.

### Macroscopic imaging

Bars from a mouse head holding device (MAG-1, Narishige) were used to head-fix the mice on a physiological monitoring station (Small Animal Physiological Monitoring System, 75-1500, Harvard Apparatus), which kept the mouse heated at 37 °C and monitored heart and respiration rate throughout the imaging. The imaging was performed at a macroscope (LAS-X software; Leica, M205FA) with a complementary metal oxide semiconductor (CMOS) camera (Hamamatsu, Orca-Flash 4.0,

C11440). For Ca$^{2+}$ recordings in GCaMP mice, a Gemini system (W-View Gemini; Hamamatsu, A12801-01) was applied to facilitate simultaneous recording in two channels. For CSF tracer distribution, imaging was performed at 5 Hz, ×1.25 zoom, 1,024 × 1,024 pixels, 16-bit, 10.4 μm per pixel. For Ca$^{2+}$ signaling, imaging was performed at 20 Hz, ×1.25 zoom, 512 × 512 pixels, 16-bit, 17.9–20.8 μm per pixel.

### Laser-Doppler flowmetry

The hemodynamic response to whisker stimulation was recorded via laser-Doppler flowmetry (Periflux 5000, 5010 LDPM, Perimed) in GLT1-GCaMP7 mice ($n = 7$, male, 18–19 weeks). First, the activated region was located via the Ca$^{2+}$ signal under the macroscope, then a laser-Doppler probe (MT B500-0L240, Perimed) was glued to the skull above the MCA vascular territory[64] and cerebral blood flow changes were recorded during whisker stimulation. The stimulation protocol varied between 1, 5 and 10 Hz with 10 ms pulse length, 10 psi for 30 s. In total, 2–6 stimulations per mouse were recorded in Clampex software (Axon pCLAMP) and averaged.

### IOS

Two days before imaging, mice were head-plated and thin-skulled above the MCA in both hemispheres under isoflurane anesthesia with lidocaine (2 mg kg$^{-1}$, local s.c.) and buprenorphine (0.05 mg kg$^{-1}$, i.p.) as analgesic ($n = 6$, 3 females and 3 males, 13–16 weeks). The skull was covered by a thin layer of superglue for protection. The mice received postoperative analgesia (carprofen, 5 mg kg$^{-1}$, s.c.) immediately after surgery and 24 h later. On day 3, the imaging was performed under KX anesthesia (100 mg kg$^{-1}$; 10 mg kg$^{-1}$, i.p.) and maintained with ketamine (50 mg kg$^{-1}$) after 30 min. The brain tissue was illuminated by collimated and filtered (FF01-530/11 and FF01-630/20, Semrock) LEDs (525 and 635 nm, CoolLED pE4000) to visualize total hemoglobin (HbT) and reduced hemoglobin (HbR), respectively. Reflected light was captured with an Andor iXon Ultra 897 EMCCD camera (Andor Instruments) mounted into a Nikon AZ100 microscope equipped with a ×1 objective (Nikon AZ Plan Apo 1×). Images (512 × 512 pixels, 16-bit, 20 μm per pixel) were acquired at 20 frames per second under alternation of the wavelength between every frame. LEDs and camera were triggered by a Master-8 pulse generator. The EMCCD camera was controlled via μManager (v2.0.0-gamma1 (ref. [65])). Unilateral whisker stimulations were given for 30 s (5 Hz (10 ms), 10 and 20 psi) via a Picospritzer (Parker) and controlled by Master-8 pulse generator that was stimulated by the Master-8 controlling light and camera. Between mice, stimulation was varied between left- and right-side whiskers. For analysis, ROIs were drawn above the barrel field cortex in both hemispheres and the motor cortex as control (Fiji, ImageJ). Data points from four recordings were averaged per mouse, and the MPIs were normalized to baseline (30 s before stimulation) and converted to percentage change ($\Delta R/R$) (MATLAB, 2020a). Percentage change in reflectance $\Delta R/R$ was converted into hemoglobin changes ($\Delta$HbT) using the Beer–Lambert law[13].

### Parenchymal spread of tracer

For assessment of the parenchymal spread of the CSF tracer in response to repeated whisker stimulations, mice were head-plated and an intracisternal cannula was implanted under KX anesthesia, as described above ($n = 7$, male, 13–19 weeks). Under a macroscope, the mice were intracisternally injected with a CSF tracer (2% TMR-labeled 3 kDa dextran; Thermo Fisher Scientific, D3308) at a rate of 2 μl min$^{-1}$ over 5 min with a syringe pump (KD Scientific, Legato 130). Tracer influxed for 5 min to reach the trunk of the MCA before unilateral whisker stimulation was applied for 30 min (5 Hz (10 ms), 10 psi for 30 s with 60 s intervals). Immediately after this, the brain was dissected out and prepared for ex vivo analysis, as described further below.

### Glymphatic clearance

Mice were head-plated and implanted with an intracisternal cannula under KX anesthesia, as described above ($n = 6$, male, 11–15 weeks).

Anesthesia was maintained, and mice were transferred to a macroscope for imaging. The mice were intracisternally injected with CSF tracer (10 µl (3 kDa) fluorescein- or 10 kDa AF647-labeled dextran, 1%; Thermo Fisher Scientific, D3306 and D22914) at a rate of 1 µl min⁻¹ over 10 min with a syringe pump (KD Scientific, Legato 130). After the injection, the tracer circulated for 30 min before whisker stimulations started (5 Hz (10 ms), 15 psi for 30 s with 60 s intervals). A total of 20 whisker stimulations were delivered over 30 min. The tracer distribution was recorded by a macroscope (LAS-X software; Leica, M205FA) before and during the whisker stimulation (60 min total; 5 Hz frame rate, ×1.25 zoom, ET GFP filter, 1,024 × 1,024 pixels, 16-bit, 10.4 µm per pixel).

### Tracer quantification in arteries and veins

Under KX anesthesia (100 mg kg⁻¹; 10 mg kg⁻¹, i.p.), NG2-dsRed mice (n = 3 per time point, male, 3–14 months) were intracisternally injected with CSF tracer (20 µl of 0.5% (wt/vol) FITC-labeled 70 kDa dextran; Thermo Fisher Scientific, D1822) at a rate of 2 µl min⁻¹ over 10 min. Anesthesia was maintained until cardiac perfusion with wheat germ agglutinin (WGA) conjugated to AF647 (WGA-647, 0.01 mg ml⁻¹; Thermo Fisher Scientific, W32466) in 20 ml PBS, followed by 20 ml paraformaldehyde (PFA, 4% in PBS) at either 30 min or 120 min after infusion start. Five minutes before cardiac perfusion, mice were given 100 µl WGA-647 (1 mg ml⁻¹; Thermo Fisher Scientific, W32466) intravenously via femoral vein injection to ensure efficient intravascular labeling. Brains were extracted and immersion fixed overnight in PFA (4% in PBS). Brains were prepared for ex vivo analysis, as described below, and imaged with a fluorescent macroscope. Multiple FOVs were acquired at 1.048 µm² per pixel and stitched together to provide an image of the entire brain section (Objective: UplanXApo ×10/numerical aperture 0.40, ∞/compatible cover glass thickness 0.17 mm per field number 26.5 mm, no immersion liquid (air), Olympus). Representative images (Fig. 3g,h and Extended Data Fig. 4f) were acquired with a confocal microscope (FluoView, Objective: UPlanXApo ×40/numerical aperture 0.95, ∞/compatible cover glass thickness 0.17 mm per field number 26.5 mm, Olympus).

Image analysis was conducted using ImageJ (NIH) and MATLAB (Mathworks). Analysis pipeline is illustrated in Extended Data Fig. 4b. First, vessels were scored for tracer presence using only the green channel of 70 kDa FITC-labeled dextran, placing points on each vessel. Next, these vessels with tracer were classified as arteries or veins using the NG2-dsRed expression pattern. Arteries exhibit ensheathing smooth muscle cells with a banded appearance, while venous smooth muscle cells lack this banded pattern (Extended Data Fig. 4f). Only vessels that could be definitively scored were included in the analysis. Any vessels that only had tracer present at the first 200 µm of the brain surface were excluded as potential perfusion artifacts. Anatomical landmarks visualized on the blue channel were used to segment each brain slice into brain subregions according to the Allen Brain Atlas.

A MATLAB script loaded all the subregion ROIs and counted the number of arteries and veins within each ROI. The counts were also pooled into more general regions, which are as follows: cortical and deep (cortical = dorsal cortex, lateral cortex and cortex; deep = corpus callosum, internal capsule, hippocampus, thalamus and hypothalamus). The proportion of arteries and veins was calculated by taking the identified arteries or veins and dividing them by the sum of arteries and veins with a tracer present for that brain region. The relative change was calculated by subtracting the mean of the proportions of the 30-min group from the proportion of each animal in the 120-min group. For each animal, three brain sections were analyzed (−1.8, −2.4 and −3.2 mm relative to bregma).

### Particle tracking experiments

Mice were anesthetized with a KX mixture (100 mg kg⁻¹; 10 mg kg⁻¹, i.p.) and fixed in a stereotaxic frame (n = 7, male, 14–16 weeks). Lidocaine (2 mg kg⁻¹, s.c.) and buprenorphine (0.05 mg kg⁻¹, i.p.) were injected for

pain management. A cranial window was carefully made above the MCA, and the brain tissue was covered with 1.1% wt/vol agarose gel with a 5 mm coverslip on top. The mice were head-plated, and an intracisternal catheter was inserted, as described above. Anesthesia was maintained, and mice were transferred to a two-photon microscope for imaging. Before imaging, an intravascular tracer (0.1 ml FITC-labeled 2,000 kDa dextran, 1%; Sigma-Aldrich, FD2000S) was injected retro-orbitally. The mouse was positioned on a mouse head holding device with angle adjuster (MAG-2, Narishiqe) for horizontal imaging of the cranial window and a heating pad maintained body temperature at 37 °C. Red fluorescent polystyrene microspheres (FluoSpheres 1.0 µm, 580/605 nm, 0.25% (1:3) in artificial CSF (aCSF), 2 µl min⁻¹; Invitrogen, F13083) were sonicated before injection into the cisterna magna during two-photon imaging (Thorlabs Bergamo B-Scope, with galvo-resonant scanning, Spectra-Physics InSight DS+ laser. Thorlabs ThorImage software) with a ×25 objective (Nikon CFI APO LWD Objective, 380–1050 nm, 1.10 NA, 2.0 mm working distance (WD)). Emission light was split by a 562-nm long-pass dichroic mirror into 525/50 nm and 607/70 nm bandpass filters (Semrock) for imaging green and red channels, respectively. The spheres were excited at 820 nm, and we recorded at a frame rate of 29.6 fps. Images had a spatial dimension of 512 × 512 pixels. Whisker stimulations were controlled by a Master-8 and delivered unilaterally at 5 Hz (10 ms), 15 psi (30 s with 60 s interval, seven stimulations per mouse).

### Glymphatic inflow during wakefulness

Before awake imaging, mice were head-plated, as described above, and the skull was covered by a thin layer of superglue for protection (n = 8, 7 females and 1 male, 11–14 weeks). The mice recovered for 2 d before being trained to awake head fixation (5 and 10 min on day 1 with >1 h between sessions; 30 min on day 2). On the following day, the mice were intracisternally cannulated, as described above, and recovered for 2 d before awake macroscope imaging. Glymphatic tracer (10 µl TMR-labeled 3 kDa dextran, 2%; D3308, Thermo Fisher Scientific) was injected at a rate of 1 µl min⁻¹ (KD Scientific, Legato 130). Tracer distribution was recorded by macroscopic imaging (LAS-X software; Leica, M205FA; 5 Hz frame rate, ×1.25 zoom, mCHER filter, 1,024 × 1,024 pixels, 16-bit, 10.4 µm per pixel). Ten minutes after cessation of injection, whisker stimulation was applied unilaterally for 30 min (30 s stimulation with 60 s intervals for a total of 20 stimulations; 5 Hz (10 ms), 20 psi). Image analysis is described below. Ex vivo sample preparation and imaging were performed as described below.

### Chronic cranial window for awake imaging

Mice were anesthetized with KX (100 mg kg⁻¹; 10 mg kg⁻¹, i.p.), and preoperative analgesia was supplied for pain management (2 mg kg⁻¹ lidocaine s.c.; 0.05 mg kg⁻¹ buprenorphine s.c.). Mice were head-plated, and a craniotomy was made above the MCA (n = 4, female, 22 weeks). After the removal of the dura, the window was sealed with a 4 mm glass coverslip. The mice received carprofen (5 mg kg⁻¹, s.c.) postoperatively and for the subsequent 3 d of recovery before adaptation to awake head fixation. Just before imaging, mice were briefly sedated with 3.5% isoflurane to facilitate retro-orbital injection of an intravascular tracer (Texas Red-labeled 70 kDa dextran, 15 mg ml⁻¹; Thermo Fisher Scientific, D1864). Mice were positioned in a MAG-2 (Narishiqe) for two-photon imaging (Thorlabs Bergamo B-Scope, with galvo-resonant scanning, Spectra-Physics InSight DS+ laser; Thorlabs ThorImage software) with a ×25 objective (Nikon CFI APO LWD Objective, 380–1,050 nm, 1.10 NA, 2.0 mm WD). Emission light was split by a 562-nm long-pass dichroic mirror into 525/50 nm and 607/70 nm bandpass filters (Semrock) for imaging green and red channels, respectively. Excitation wavelength was set to 960 nm, and recordings were performed at a frame rate of 30 fps (512 × 512 pixels).

For analysis, we applied custom-written segmentation codes to segment endfeet from each other and the background. After making

the segmented images binary, we found the graphic centroid for the artery and the endfeet. We measured the distance between the centroid of the artery and the centroid of the endfeet to register the relative movement of the endfeet from the artery during functional hyperemia.

### Stereotaxic adeno-associated virus (AAV) injections

Virus injection was performed with a Hamilton syringe mounted to a micromanipulator (World Precision Instruments) at a 10-degree angle. At the coordinates A/P: −2.98 mm, M/L: −3.00 mm from bregma, a concentration of $2.5 \times 10^{11} - 1 \times 10^{13}$ GC ml$^{-1}$ was injected of virus ssAAV-PHP. eB/2-GFAP(2.2)-mClY-WPRE-bGHp(A) (Viral Vector Facility, Neuroscience Center Zurich)[66]. Animals were imaged 2–4 weeks after injection and after a craniotomy was performed.

### Optogenetic activation of pial arteries

We generated the mouse line Sm22-Cre:Ai32-ChR2 expressing ChR2 in the smooth muscle cells to study the cerebral arteries. Upon photoactivation, the intracellular Ca$^{2+}$ concentration increases, depolarizes the smooth muscle cells and induces constriction of the artery. Mice were anesthetized with KX (100 mg kg$^{-1}$; 10 mg kg$^{-1}$, i.p.) and fixed in a stereotaxic frame before head-plating and insertion of an intracisternal catheter, as described above ($n = 6$, 8–14 weeks). Lidocaine (2 mg kg$^{-1}$, s.c.) and buprenorphine (0.05 mg kg$^{-1}$, i.p.) were injected for pain management. Anesthesia was maintained, and mice were transferred to an epifluorescence macroscope (LAS-X software; Leica, M205FA) with a ×1.0 objective (Planapo M-series, Leica) and an CMOS camera (ORCA-Flash4.0 V2, Hamamatsu Photonics) for in vivo recordings. Fluorescent CSF tracer (10 μl TRITC-labeled 2,000 kDa dextran, 2%; Sigma-Aldrich, 73766) was injected at 2 μl min$^{-1}$ into the cisterna magna. When the CSF tracer appeared at the MCA, an optic probe (Thorlabs) was placed at the proximal part of the MCA. Stimulation light (MBL-FN-473-200mW, CNI laser) was set to 5 and applied through the skull (473 nm, 10 Hz (50 ms)) for 30 s with 30 s interval for a total of 30 min. Optogenetic stimulation was controlled by a USB hub (OTPG_8, Doric). Imaging was acquired at 5 Hz (1,024 × 1,024, 16-bit). At the end of the experiment, brains were dissected out and immersion fixed in 4% PFA overnight. Brains were prepared for ex vivo analysis, as described below, and imaged on a macroscope (Olympus MVX10 with a PRIOR Lumen LED and Hamamatsu ORCA-Flash4.0 V2 Digital CMOS camera) using a Texas Red filter set (Metamorph software).

### Optogenetic particle tracking

For particle tracking analysis in optogenetic mice, mice were head-plated, implanted with an intracisternal catheter and a cranial window was carefully made above the MCA under KX anesthesia, as described above ($n = 5$, 3 female, 2 male, 9–15 weeks). Anesthesia was maintained, and mice were transferred to a macroscope for in vivo imaging ((LAS-X software; Leica, M205FA) with a CMOS camera (Orca-Flash 4.0; Hamamatsu, C11440)). Crimson fluorescent polystyrene microspheres (FluoSpheres 1.0 μm, 625/645 nm, 0.125% (1:7) in aCSF, 2 μl min$^{-1}$; Invitrogen, F8816) were sonicated before injection into the cisterna magna. Imaging was acquired at 5 Hz, ×5−6 zoom, 1,024 × 1,024 pixels, 16-bit, 1.68–2.6 μm per pixel. An optic probe was placed in the middle of the imaged MCA segment. Stimulation light (CNI laser, MBL-FN-473-200mW) was set to 5 (1–2.5 mW) and applied through the cranial window (473 nm, 10 Hz (50 ms)) for 30 s with 60 s interval.

### Ex vivo sample preparation

For ex vivo analysis of parenchymal tracer distribution, the brain was rapidly dissected out and immersion fixed in 4% PFA overnight before sectioning on a vibratome (Leica, VT1200S). During sectioning, the brain was bathed in cold PBS and the chamber was kept cold with ice. Sections were 100-μm thick, cut at a speed of 0.6 mm s$^{-1}$ and an amplitude of 1 mm. The sections were stained free-floating with DAPI (Thermo

Fisher Scientific, 62248; 1:1,000 in PBS) for 5 min before mounting with ProLong Gold Antifade mounting medium (Thermo Fisher Scientific, P36934) on glass slides and covered with coverslips (Hounisen).

**Epifluorescence imaging of tissue sections.** For each mouse, eight sections between 0.3 and −1.7 mm from bregma were chosen for imaging and analysis. They were acquired on a Nikon epifluorescence microscope with the ND Acquisition tool of Nikon (NIS Elements AR) with a ×4 objective and automated stitching. Subsequent analysis was performed in ImageJ software (NIH) with uniform thresholding. ROIs were drawn around each hemisphere or the cortices to measure MPI. The total tracer signal in each slice was set to 100%, and we calculated the percentage of tracer distributed into each hemisphere.

**Analysis of in vivo glymphatic activity.** For analysis of in vivo glymphatic activity, an ROI was drawn above the MCA in each hemisphere and MPI was extracted for the 30 min influx period (MATLAB). Every trace (90 s) was normalized to the tracer signal at stimulation start ($t = 30$ s). For each mouse, all traces ($n = 20$) were averaged across the whisker stimulation.

**Peristimulus analysis of Ca$^{2+}$ signals.** Thy1-GCaMP6S mice received unilateral whisker stimulations while imaging the Ca$^{2+}$ signal. To enhance the Ca$^{2+}$ signal, each whisker stimulation protocol was recorded six consecutive times and the videos (90 s each) were averaged in MATLAB. In ImageJ (Fiji), an average z projection was created and subtracted as background. ROIs were drawn above the barrel field cortex of both hemispheres to extract the z-axis profiles.

**Particle tracking analysis.** Image processing method. First, image registration of each image in the time series was performed to correct the movement of the mouse. Via rigid translation, the image registration algorithm in MATLAB has an accuracy of 0.2 pixels. Manual correction by linear interpolation was applied when necessary to correct erroneous correlations in the translation. The edges of each image were padded with zero-valued pixels to maintain a homogeneous spatial extent.

**PTV analysis.** We tracked microspheres in the red channel. To measure CSF flow velocity profiles, we used a custom-built, automated particle tracking software in MATLAB[18]. The algorithm locates each microsphere with subpixel accuracy, tracks it through time and calculates its velocity in each frame. We identified and masked stagnant microspheres stuck on the vessel wall by setting a threshold for the lowest mean velocity or masking manually. The domain was divided into approximately 70 × 70 boxes with a resolution of 7.5 × 7.5 pixels each.

The downstream velocity component was calculated as $u \cdot u_{avg}$, and the cross-stream velocity component was calculated as $|u \times u_{avg}|$, where $u$ is the particle velocity and $u_{avg}$ is the time-averaged velocity field, normalized to unit length.

**Artery and PVS width and wall velocity measurement.** A MATLAB algorithm was used to measure the artery and PVS width changes during whisker stimulations. two-photon recordings with CSF (10 μl TMR-labeled 3 kDa dextran, 2%; Invitrogen, D3308) and intravascular tracers (0.1 ml FITC-labeled 2,000 kDa dextran, 1%; Sigma-Aldrich, FD2000S) were used. For measurements of the artery diameter, a centerline of the vessel was selected manually based on the red fluorescence channel. Five evenly spaced lines were drawn along the centerline's perpendicular direction, and the vessel diameter was measured across each. The algorithm automatically detected the boundary of the artery based on the sharp change in pixel intensity. The same method was applied to measure the width of the PVS. For measurements of the outer perivascular membrane, a line was drawn across the artery and PVSs on both sides. We calculated the artery wall velocity by numerically differentiating the wall position. The time step $\Delta t$ was $\frac{1}{fps}$,

where fps is the frame rate of the recordings. We applied a Gaussian filter to smooth the wall velocity signal using a kernel size of 3 s.

For the cross-correlation analysis between the vessel wall velocity, the vessel diameter and the CSF flow velocity during stimulation, we used the 'xcorr.m' function, a built-in MATLAB function.

**Front-tracking analysis.** We tracked fronts using an automated MAT-LAB algorithm developed at the University of Rochester. Fronts are curves that separate bright regions from dark regions in macroscopic videos. Local front speeds quantify the local speeds of CSF tracer influx. We kept the brightness threshold uniform for both hemispheres and measured the mean front velocity over 10 min. We lowered the threshold for the unstimulated hemisphere if the front was too dim compared to that of the stimulated hemisphere.

**Impedance pumping models.** Flows driven by arterial diameter changes were modeled via IB2D, an open-source, 2D immersed boundary method code for fluid simulation. Approximating arterial diameter changes and flow to be axially symmetric, we modeled an axial plane of the artery and PVS. In a $5 \times 5$ nondimensional computational domain with periodic boundary conditions, we modeled each tissue (upper and lower artery wall, upper and lower PVS boundary) as a single layer of solid nodes spanning $1 \le x \le 4$, where $x$ is the axial coordinate and $x = 0$ at the left end of the domain. In dimensionless units, the diameter of the artery was 2 and the diameter of the PVS was 3.1, such that the ratio of their cross-sectional areas was 1:1.4 as measured in vivo[18]. We defined the artery walls as deformable tissues with spring stiffness $k = 5 \times 10^5$ and beam stiffness $k_b = 1 \times 10^7$. The upper and bottom artery walls were linked with spring stiffness $k_{s1} = k_s/100$ to account for their connection in three dimensions. The left and right ends of the artery walls were fixed in place, as were the entire PVS outer boundaries.

The grid size of the CSF fluid was $64 \times 64$, and that of the solid tissues was $128 \times 1$. The time step of the simulation was $dt = 5 \times 10^{-4}$. We drove arterial diameter changes by applying a uniform force over the region $1.39 \le x \le 2.17$, which varied over time.

$$F = \begin{cases} 2k_{s1}\Delta D \sin^2 \frac{2\pi}{4(t_2-t_1)}(t-t_1), & t_1 \le t < t_2 \\ 2k_{s1}\Delta D, & t_2 \le t < t_3 \\ 2k_{s1}\Delta D(1 - \sin^2 \frac{2\pi}{4(t_4-t_3)}(t-t_3)), & t_3 \le t < t_4 \end{cases}$$

Otherwise, $F = 0$. Here $t$ is time, $\Delta D = 0.05$ for dilation and $-0.05$ for constriction, $t_1 = 0.025$, $t_2 = 0.03125$, $t_3 = 0.04375$ and $t_4 = 0.05$. The motion of the artery walls and the CSF were calculated based on the applied force, the elastic forces of tissues and the interactive forces between tissues and fluids. The normalized force $\frac{F}{k_{s1}}$ is plotted in red in Fig. 8d,j.

We calculated the 2D volume flow rate through a cross-section of the PVS via numerical integration as $Q = \int_\Gamma U(r)\,dr$, where $U$ is the axial velocity, $\Gamma$ is the cross-section and $r$ is the radial coordinate. We calculated the normalized net mass flux of CSF as $\int_\tau Q\,dt$. We also simulated tracers in the PVS, which move exactly as fluid elements, to visualize the Lagrangian movement of the CSF.

**CSF flow rate measurements.** Flux estimation during baseline CSF flow. We performed CSF flow rate estimations based on our two-photon and macroscopic imaging. We overlapped all particle tracks in our two-photon recordings to visualize the PVS and measure its time-averaged outer diameter. We modeled the vessel wall and the outer boundary of the PVS as concentric cylinders. We measured the baseline mean flow rate of CSF over time by multiplying the mean downstream velocity component with the cross-sectional area of the PVS. The baseline mean flow rate $f_{baseline}$ across the PVS is

given as $f_{baseline} = u_{down} \cdot \pi \cdot \frac{D_{PVS}^2 - D_{Ves}^2}{4}$, where $u_{down}$ is the downstream velocity, $D_{PVS}$ is the outer diameter of the PVS and $D_{Ves}$ is the vessel diameter.

**Flux estimation in the stimulated hemisphere.** During the injection, when tracer influx is significant and efflux is negligible, the mass of tracers transported across the pial PVS must equal the mass of tracers that accumulate in the hemisphere:

$$m_{tracer} = \int_0^t C_{PVS} \cdot f\,dt = \int C_{brain}\,dV$$

Here $m_{tracer}$ is the mass of tracer, $C_{PVS}$ is the tracer concentration in the PVS, $f$ is the mean volume flow rate and $C_{brain}$ is the tracer concentration in the brain. By taking a time derivative and assuming that the tracers distribute evenly in the brain, we find

$$\frac{dm_{tracer}}{dt} = C_{PVS} \cdot f = \frac{dC_{brain}}{dt} \cdot V_{brain}$$

which applies separately to both the stimulated and unstimulated hemispheres. Considering the ratio of the equations for the two hemispheres, assuming that tracer concentration is proportional to image intensity and assuming that the two hemispheres have equal volume, we find

$$\frac{f_{stim}}{f_{unstim}} = \frac{\frac{d(MPI_{stim})}{dt}}{\frac{d(MPI_{unstim})}{dt}}$$

where $f_{stim}$ and $f_{unstim}$ are the volume flow rates to the stimulated and unstimulated hemispheres, respectively, and $MPI_{stim}$ and $MPI_{unstim}$ are the MPI in the stimulated and unstimulated hemispheres, respectively. $f_{unstim}$ is given by the baseline mean flow measurement $f_{baseline}$ in the previous section. We can determine $\frac{d(MPI_{stim,hemi})}{dt}$ and $\frac{d(MPI_{unstim,hemi})}{dt}$ from Fig. 1e by calculating the slope of each curve using a linear fit from $t = 0$ min to $t = 20$ min, an interval chosen to ensure that influx dominates efflux, consistent with our assumption above. Therefore, we can estimate the flow rate during functional hyperemia in the stimulated hemisphere.

**Statistics and reproducibility.** Animals in test and control groups were randomly selected. No statistical methods were used to predetermine sample sizes, but our sample sizes are similar to those reported in previous publications[1,5,18]. For Fig. 2b,c, tracer distribution along arteries and veins was blindly scored. Data collection and analysis for the rest of the study were not performed blind due to the conditions of the experiments. Poor imaging quality led to exclusion. Data distribution was assumed to be normal, but this was not formally tested. Representative images were replicated independently with similar results with $n$ up to ten animals. Statistical tests were performed with the software Prism 9 (GraphPad) or MATLAB (2021a), and the treatment of each dataset is described in the corresponding figure legend. A $P$ value of <0.05 was considered significant. $T$-tests were two-sided. Data are presented as mean ± s.e.m.

**Reporting summary**
Further information on research design is available in the Nature Portfolio Reporting Summary linked to this article.

## Data availability
The datasets generated in this study are available from the corresponding author upon reasonable request. Source data are provided with this paper. We used the Allen Brain Atlas: Mouse Brain for anatomical reference.

## Code availability

All relevant codes are available from the corresponding author upon request.

## References

59. Monai, H. et al. Calcium imaging reveals glial involvement in transcranial direct current stimulation-induced plasticity in mouse brain. *Nat. Commun.* **7**, 11100 (2016).
60. Zhu, X., Bergles, D. E. & Nishiyama, A. NG2 cells generate both oligodendrocytes and gray matter astrocytes. *Development* **135**, 145–157 (2008).
61. Xavier, A. L. R. et al. Cannula implantation into the cisterna magna of rodents. *J. Vis. Exp.* **2018**, 57378 (2018).
62. Mestre, H., Mori, Y. & Nedergaard, M. The brain's glymphatic system: current controversies. *Trends Neurosci.* **43**, 458–466 (2020).
63. Raghunandan, A. et al. Bulk flow of cerebrospinal fluid observed in periarterial spaces is not an artifact of injection. *eLife* **10**, e65958 (2021).
64. Mestre, H. et al. Cerebrospinal fluid influx drives acute ischemic tissue swelling. *Science* **367**, eaax7171 (2020).
65. Edelstein, A. D. et al. Advanced methods of microscope control using μManager software. *J. Biol. Methods* **1**, e10 (2014).
66. Zhong, S., Navaratnam, D. & Santos-Sacchi, J. A genetically-encoded YFP sensor with enhanced chloride sensitivity, photostability and reduced pH interference demonstrates augmented transmembrane chloride movement by Gerbil Prestin (SLC26a5). *PLoS One* **9**, e99095 (2014).

## Author contributions

M.N. and S.H-R. conceived of the study and wrote the manuscript. S.H-R. planned and carried out the experiments, analyzed and interpreted data. Y.G. and D.H.K. analyzed data and developed the impedance pumping model. M.K.R., M.G. and V.U. planned and executed experiments. F.R.M.B. planned experiments and analyzed data. L.H. analyzed data. B.S. and L.R. developed analyses and analyzed data. All authors have reviewed the manuscript.

## Competing interests

All authors have no conflict of interest to declare.

## Additional information

**Extended data** is available for this paper at https://doi.org/10.1038/s41593-023-01327-2.

**Supplementary information** The online version contains supplementary material available at https://doi.org/10.1038/s41593-023-01327-2.

**Correspondence and requests for materials** should be addressed to Maiken Nedergaard.

**Peer review information** *Nature Neuroscience* thanks Anna Devor and the other, anonymous, reviewer(s) for their contribution to the peer review of this work.

**Reprints and permissions information** is available at www.nature.com/reprints.
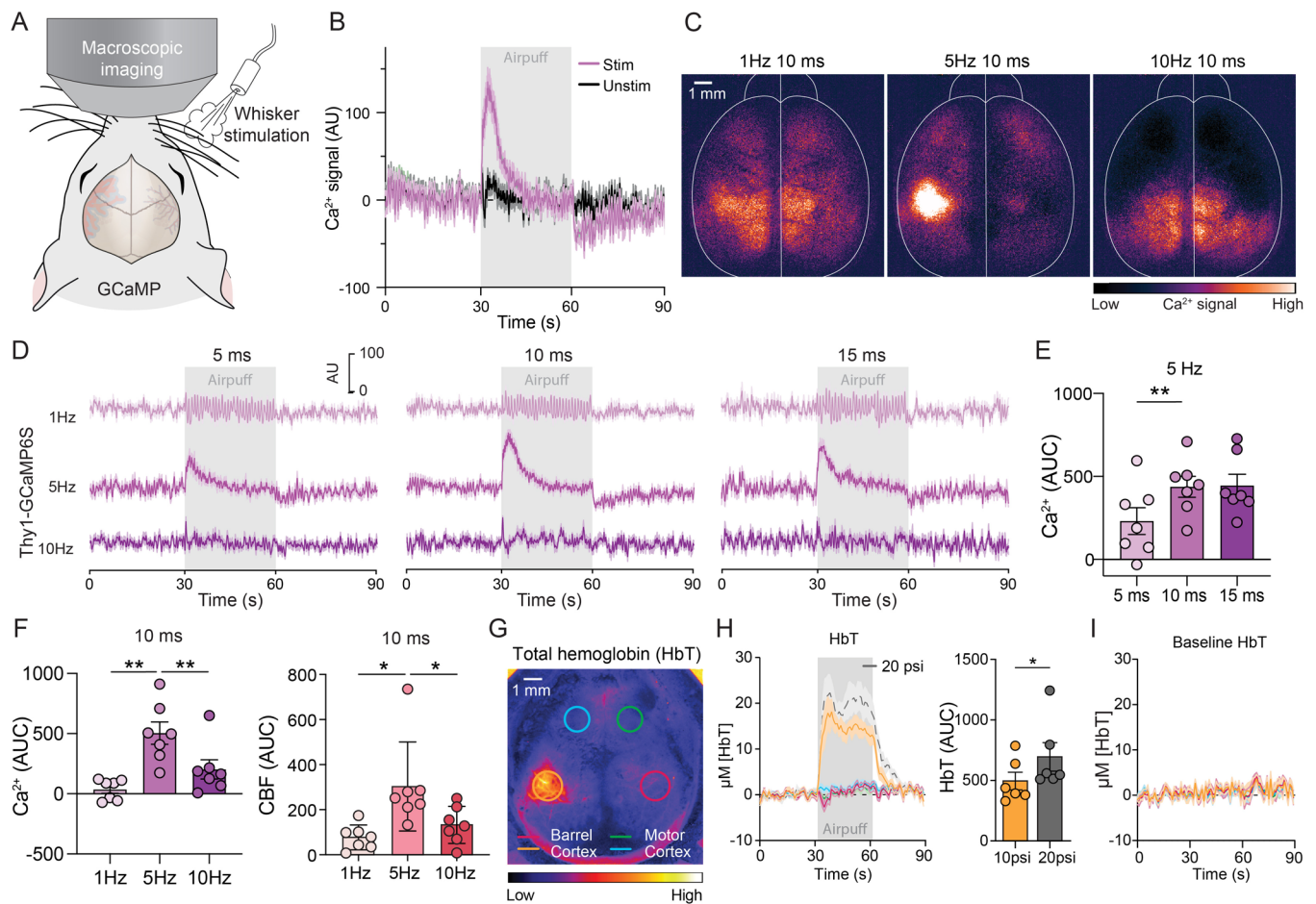
**Extended Data Fig. 1 | Whisker stimulation causes Ca²⁺ and hemodynamic responses in contralateral barrel cortex. a**. Adult wild-type mice were head-plated under ketamine/xylazine anesthesia and exposed to unilateral whisker stimulation (5 Hz 10 ms, 10 psi, 30 seconds per stimulation). Macroscopic imaging was utilized to map neuronal activation (Ca²⁺ signaling) in GCaMP mice. **b**. The Ca²⁺ response in the stimulated and unstimulated hemisphere across whisker stimulation in Thy1-GCaMP6S mice (n = 8 mice). **c**. Representative images of the Ca²⁺-response to three different whisker stimulation protocols (1, 5 or 10 Hz with 10 ms pulse length). The image is averaged across five stimulations. **d**. Ca²⁺ traces from barrel field cortex in response to 30 sec whisker stimulation protocols in Thy1-GCaMP6S mice (frequencies: 1, 5 or 10 Hz and pulse lengths: 5, 10 or 15 ms) (n = 7 for 5 and 10 ms, n = 5 for 15 ms). **e**. Area under the curve (AUC) of tested pulse lengths (5, 10 or 15 ms, 5 Hz) (n = 7 mice). One-way ANOVA w Tukey's correction: $P = 0.0097$, 5 vs. 10 ms; $P = 0.16$, 5 vs. 15 ms; $P = 0.99$, 10 vs. 15 ms. **f**,

AUC of traces from Fig. 1c comparing the effect of the three stimulation protocols on Ca²⁺-signaling (left) or cerebral blood flow (right) (n = 7). One-way ANOVA w Dunnett's correction: Ca²⁺: $P = 0.005$, 1 vs. 5 Hz; $P = 0.17$, 1 vs. 10 Hz; $P = 0.006$, 5 vs. 10 Hz. CBF: $P = 0.04$, 1 vs. 5 Hz; $P = 0.04$, 5 vs. 10 Hz. **g**. The total hemoglobin (HbT) change in barrel cortex in response to unilateral whisker stimulation (5 Hz 10 ms, 10 psi). Regions of interest (ROI) are depicted above barrel and motor cortex in both hemispheres. **h**. The hemodynamic response during whisker stimulation in barrel cortex (pink and orange) and in control regions (green and blue). The gray dashed line represents the HbT response in the stimulated barrel cortex (orange), when elevating the air pressure from 10 to 20 psi. Right: AUC of the HbT in barrel field cortex, when applying air pressure of 10 or 20 psi (n = 6 mice). Two-tailed paired t-test: $P = 0.013$. **I**. Hemodynamic response in the same mice before application of any whisker stimulation. Data are represented as mean ± SEM. *=$P < 0.05$, **=$P < 0.01$.
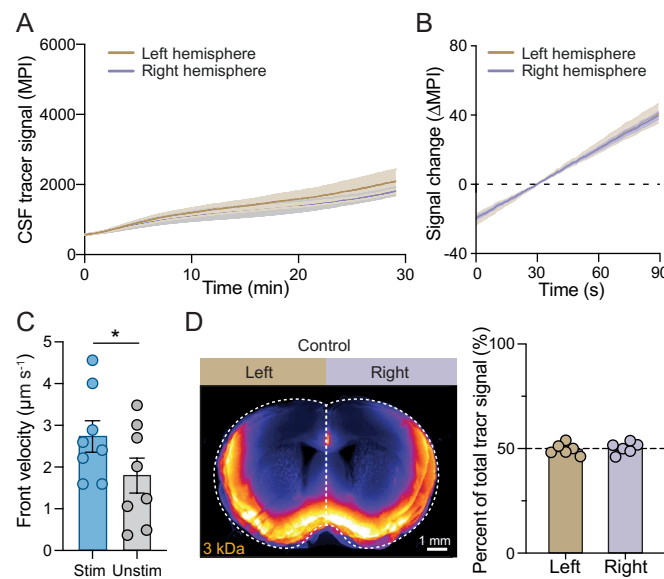
**Extended Data Fig. 2 | CSF tracer influx is symmetric across the hemispheres in control non-stimulated mice. a**. Fluorescence signal (mean pixel intensity (MPI)) of the CSF tracer (70 kDa dextran) in each hemisphere of the control mice (n = 7). **b**. Average fluorescent signal change across 90 seconds in left and right hemisphere of control mice receiving no whisker stimulation (n = 7). Normalized according to tracer intensity at stimulation start (t = 30 seconds). **c**. Front-tracking of the CSF tracer spread during macroscopic imaging demonstrates higher velocity in the stimulated hemisphere (n = 8). Two mice from Fig. 1e were not eligible for front-tracking analysis. Two-tailed paired t-test: *P* = 0.033. **d**. Left: Group overlay of the fluorescent signal displaying the parenchymal influx of the CSF tracer in *ex vivo* brain sections spanning the barrel cortex area (anterior/posterior (A/P): 0.3 to -1.7) in control mice receiving no whisker stimulations. Each hemisphere was analyzed (regions of interest are outlined by white dotted lines). Right: Percentage distribution of tracer (3 kDa dextran) in the two hemispheres (49.7 ± 1.1% vs. 50.3 ± 1.1%). The total tracer signal in each brain was set to 100% (n = 6). Two-tailed paired t-test: *P* = 0.77. Data are represented as mean ± SEM. *=P < 0.05.
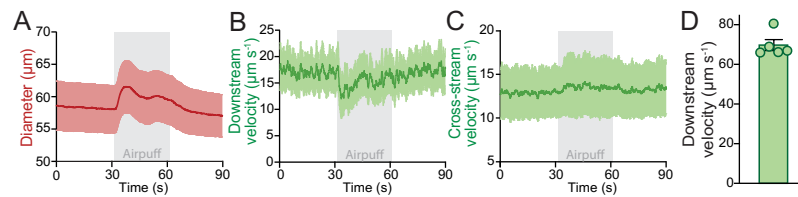
**Extended Data Fig. 3 | Puncture of the perivascular space membrane increases CSF flow velocity. a**–**c**. Absolute values of the average change in pial artery diameter (a), downstream CSF flow velocity (b) and cross-stream CSF flow velocity (c) during functional hyperemia (n = 7). **d**. The downstream velocity increases dramatically in mice with punctured perivascular space membrane (n = 5). Mean CSF flow velocity: 70.5 ± 3.8 μm/s.
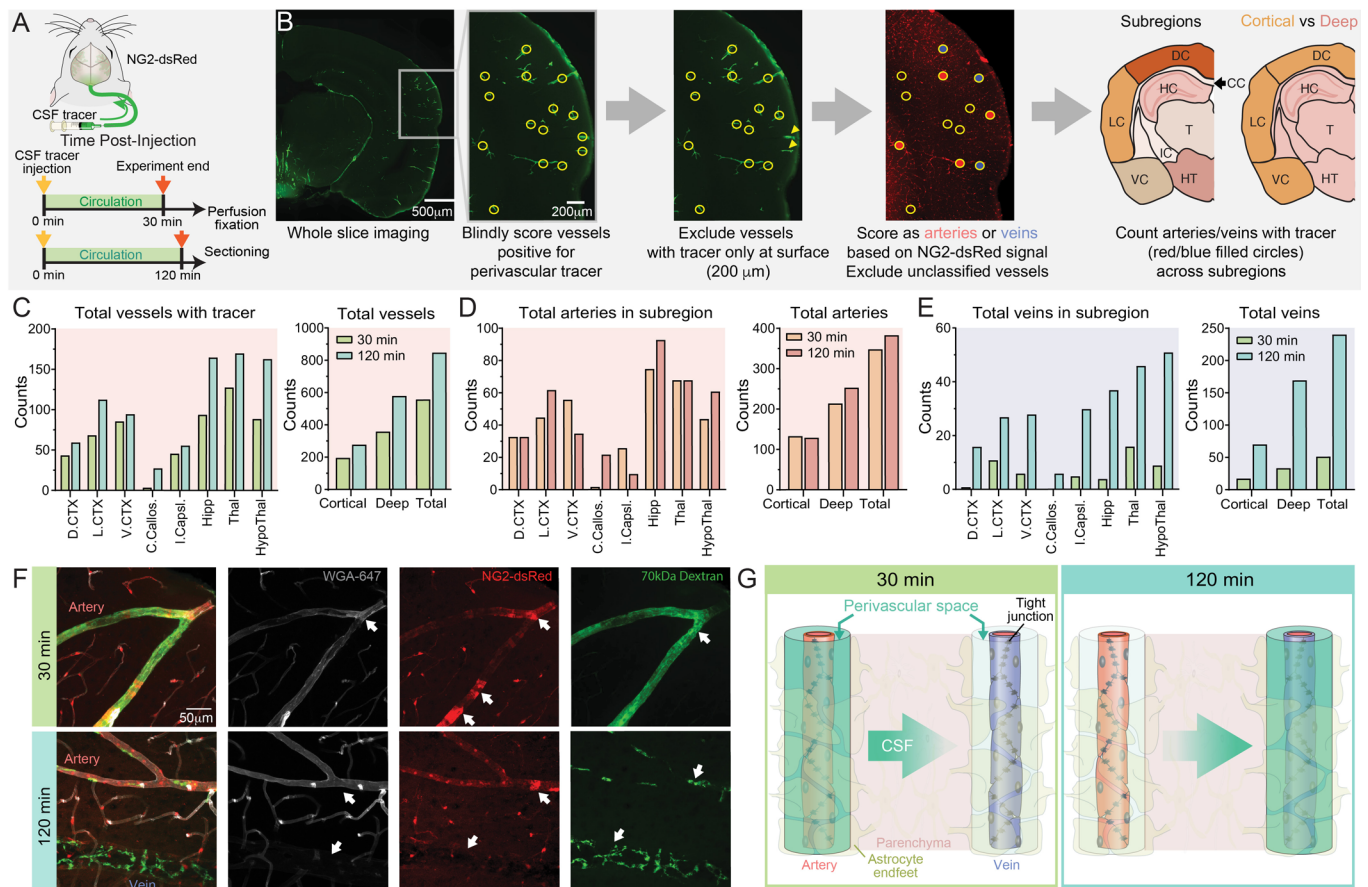
**Extended Data Fig. 4 | CSF tracer moves from arterial to venous perivascular spaces over time. a**. Adult NG2-dsRed mice were intracisternally injected (70 kDa dextran) under ketamine/xylazine anesthesia. At 30 or 120 minutes after infusion start, mice were intracardially perfused with lectin (WGA-647) followed by 4% paraformaldehyde (PFA). **b**. Representative section from 120 min group (-2.4 mm bregma), inset = lateral cortex. Analysis pipeline from left to right: vessels were scored as positive for perivascular CSF tracer (yellow circles). Vessels were excluded if there was no tracer deeper than 200 μm from the brain surface (arrowheads). Using NG2-dsRed, vessels were scored as arteries (red) or veins (blue) if they had banded or diffuse dsRed signal, respectively. Finally, the number of arteries and veins with tracer was counted for each brain region. **c**–**e**. Number of vessels (c) (scored as arteries/veins as well as uncategorized),

arteries (d), or veins (e) with CSF tracer at each brain subregion (left), and pooled into cortical, deep, and total (right) (3 brain sections/mouse; -1.8, -2.4, and -3.2 mm bregma) (n = 3). **f**. Representative images of tracer distribution in arteries from lateral cortex at 30 minutes (top) and 120 minutes (bottom). WGA-647 labeling is high in arteries (arrows), but low in veins. NG2-dsRed signal is banded in arteries (arrows) and diffuse in veins. CSF tracer (70 kDa dextran) concentration in arterial perivascular spaces is high at 30 minutes (arrow, top panel), and in part phagocytosed by perivascular macrophages around arteries and veins at 120 minutes (bottom panel). **g**. Model diagram depicting high CSF tracer at arterial perivascular spaces at 30 minutes, and high CSF tracer at venous perivascular spaces at 120 minutes post infusion. Data are represented as mean ± SEM.
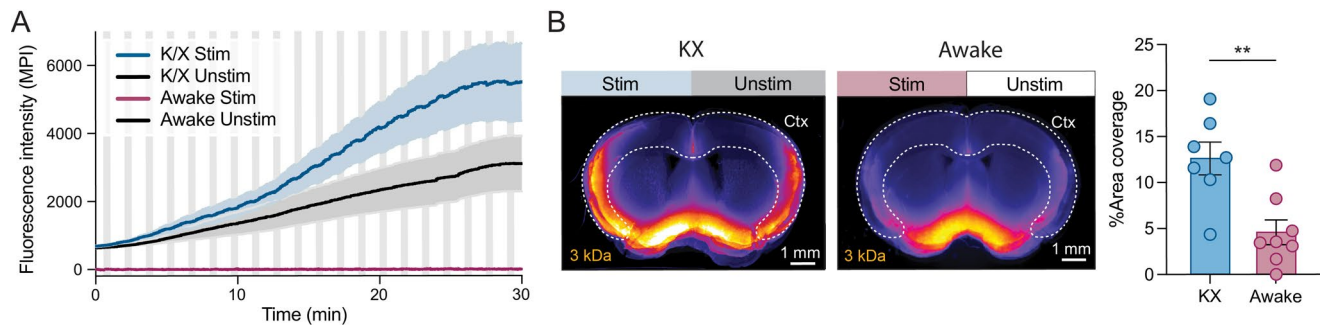
**Extended Data Fig. 5 | Tracer inflow and parenchymal spread is larger in anesthetized compared to awake mice. a**. Overlay of Figs. 1e and 4d: CSF tracer signal (mean pixel intensity (MPI)) across 30 minutes in the stimulated and unstimulated hemisphere of both anesthetized (n = 10) and awake mice (n = 8) in response to whisker stimulations. Gray bars: 30 sec whisker stimulation.

**b**. Parenchymal spread of CSF tracer in the cortices (ROI outlined by white dotted lines) in anesthetized (n = 7) and awake mice (n = 8) measured as the %Area coverage (12.6 ± 1.8% vs. 4.6 ± 1.5%). Two-way ANOVA with Sidak correction, $P = 0.0029$. Data are represented as mean ± SEM. **=$P < 0.01$.
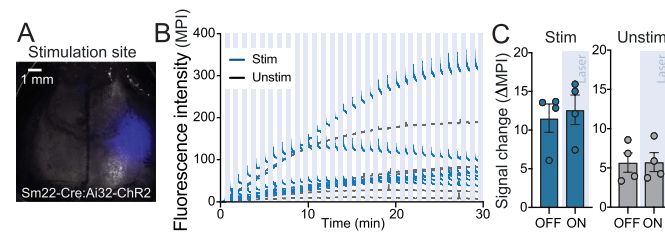
**Extended Data Fig. 6 | Optogenetic stimulation increases total tracer influx. a**. Representative image of optogenetic stimulation above the middle cerebral artery in Sm22-Cre:Ai32-ChR2 mice. **b**. The individual traces from the optogenetic mice shown in Fig. 5c (n = 6). Blue bars: laser stimulation (30 seconds each; 10 Hz 50 ms). **c**. Average change in tracer signal (mean pixel intensity (MPI)) during and between stimulations in control animals (Sm22-Cre$^{-/-}$:Ai32-ChR2) (n = 4). Two-way ANOVA with Sidak correction, $P = 0.83$, stim; $P = 0.99$, unstim. Data are represented as mean ± SEM.

# nature portfolio

Corresponding author(s): Maiken Nedergaard

Last updated by author(s): Mar 26, 2023

# Reporting Summary

Nature Portfolio wishes to improve the reproducibility of the work that we publish. This form provides structure for consistency and transparency in reporting. For further information on Nature Portfolio policies, see our Editorial Policies and the Editorial Policy Checklist.

## Statistics

For all statistical analyses, confirm that the following items are present in the figure legend, table legend, main text, or Methods section.

| n/a | Confirmed | |
|---|---|---|
| ☐ | ☒ | The exact sample size (*n*) for each experimental group/condition, given as a discrete number and unit of measurement |
| ☐ | ☒ | A statement on whether measurements were taken from distinct samples or whether the same sample was measured repeatedly |
| ☐ | ☒ | The statistical test(s) used AND whether they are one- or two-sided *Only common tests should be described solely by name; describe more complex techniques in the Methods section.* |
| ☒ | ☐ | A description of all covariates tested |
| ☐ | ☒ | A description of any assumptions or corrections, such as tests of normality and adjustment for multiple comparisons |
| ☐ | ☒ | A full description of the statistical parameters including central tendency (e.g. means) or other basic estimates (e.g. regression coefficient) AND variation (e.g. standard deviation) or associated estimates of uncertainty (e.g. confidence intervals) |
| ☐ | ☒ | For null hypothesis testing, the test statistic (e.g. $F$, $t$, $r$) with confidence intervals, effect sizes, degrees of freedom and $P$ value noted *Give P values as exact values whenever suitable.* |
| ☒ | ☐ | For Bayesian analysis, information on the choice of priors and Markov chain Monte Carlo settings |
| ☒ | ☐ | For hierarchical and complex designs, identification of the appropriate level for tests and full reporting of outcomes |
| ☒ | ☐ | Estimates of effect sizes (e.g. Cohen's *d*, Pearson's *r*), indicating how they were calculated |

*Our web collection on statistics for biologists contains articles on many of the points above.*

## Software and code

Policy information about availability of computer code

| Data collection | Clampex software (Axon™ pCLAMP). LAS X software (for Leica stereo microscope, M 205 FA). ThorLabs ThorImage software (for 2-photon imaging). Metamorph software. Nikon NIS Elements AR. |
|---|---|
| Data analysis | Fiji (ImageJ). Matlab (2020a and 2021a). GraphPad Prism 9. |

For manuscripts utilizing custom algorithms or software that are central to the research but not yet described in published literature, software must be made available to editors and reviewers. We strongly encourage code deposition in a community repository (e.g. GitHub). See the Nature Portfolio guidelines for submitting code & software for further information.

## Data

Policy information about availability of data

All manuscripts must include a data availability statement. This statement should provide the following information, where applicable:
- Accession codes, unique identifiers, or web links for publicly available datasets
- A description of any restrictions on data availability
- For clinical datasets or third party data, please ensure that the statement adheres to our policy

Source data are provided with this paper. The datasets generated in this study are available from the corresponding author upon reasonable request. We used the Allen Brain Atlas: Mouse Brain for anatomical reference.

# Human research participants

Policy information about studies involving human research participants and Sex and Gender in Research.

| | |
|---|---|
| Reporting on sex and gender | N/A |
| Population characteristics | N/A |
| Recruitment | N/A |
| Ethics oversight | N/A |

Note that full information on the approval of the study protocol must also be provided in the manuscript.

# Field-specific reporting

Please select the one below that is the best fit for your research. If you are not sure, read the appropriate sections before making your selection.

☒ Life sciences   ☐ Behavioural & social sciences   ☐ Ecological, evolutionary & environmental sciences

For a reference copy of the document with all sections, see nature.com/documents/nr-reporting-summary-flat.pdf

# Life sciences study design

All studies must disclose on these points even when the disclosure is negative.

| | |
|---|---|
| Sample size | No statistical methods were used to predetermine sample size in these studies, but our sample sizes are similar to those reported in previous publications and the animal-to-animal variability observed during the experiments. Mestre et al. 2018. Nature Communications. Doi: 10.1038/s41467-018-0731. Rungta et al. 2018. Neuron. Doi: 10.1016/j.neuron.2018.06.012. Wang et al. 2006. Nature Neuroscience. Doi: 10.1038/nn1703. |
| Data exclusions | Poor imaging quality led to exclusion. |
| Replication | Findings on increased CSF tracer influx in response to whisker stimulations has been replicated in two separate cohorts successfully. The effect of optogenetic stimulation on CSF flow dynamics were replicated in two different cohorts successfully. |
| Randomization | Animals in test and control groups were littermates and randomly selected. |
| Blinding | For Figure 2B-C, tracer distribution along arteries and veins were blindly scored. Data collection and analysis for the rest of the study were not performed blind due to the conditions of the experiments |

# Reporting for specific materials, systems and methods

We require information from authors about some types of materials, experimental systems and methods used in many studies. Here, indicate whether each material, system or method listed is relevant to your study. If you are not sure if a list item applies to your research, read the appropriate section before selecting a response.

## Materials & experimental systems

| n/a | Involved in the study |
|---|---|
| ☒ | Antibodies |
| ☒ | Eukaryotic cell lines |
| ☒ | Palaeontology and archaeology |
| ☐ | ☒ Animals and other organisms |
| ☒ | Clinical data |
| ☒ | Dual use research of concern |

## Methods

| n/a | Involved in the study |
|---|---|
| ☒ | ChIP-seq |
| ☒ | Flow cytometry |
| ☒ | MRI-based neuroimaging |

# Animals and other research organisms

Policy information about [studies involving animals](#); [ARRIVE guidelines](#) recommended for reporting animal research, and [Sex and Gender in Research](#)

| | |
|---|---|
| Laboratory animals | Mus musculus. Strains used: C57BL/6JRj, GLT1-GCaMP7, Thy1-GCaMP6S, Sm22-Cre:Ai32-ChR2 and Sm22-Cre-/-:Ai32-ChR2. 9-22 weeks old. NG2-dsRed, 3-14 mths old. |
| Wild animals | The study did not involve wild animals. |
| Reporting on sex | Sex differences were not considered in this study, animals of both sex were included. |
| Field-collected samples | The study did not involve samples collected from the field. |
| Ethics oversight | All experiments conducted at University of Copenhagen were approved by the Danish Animal Experiments Inspectorate and were overseen by the University of Copenhagen Institutional Animal Care and Use Committee (IACUC), in compliance with the European Communities Council Directive of 22 September 2010 (2010/63/EU) legislation governing the protection of animals used for scientific purposes. All experiments conducted at the University of Rochester were approved by the University Committee on Animal Resources of the University of Rochester Medical Center and an effort was made to minimize the number of animals used. |

Note that full information on the approval of the study protocol must also be provided in the manuscript.